Article

A Structural Mimic of Carbonic Anhydrase in a Metal-Organic Framework

+CO$_2$

Zn-OH → Zn-OCOOH

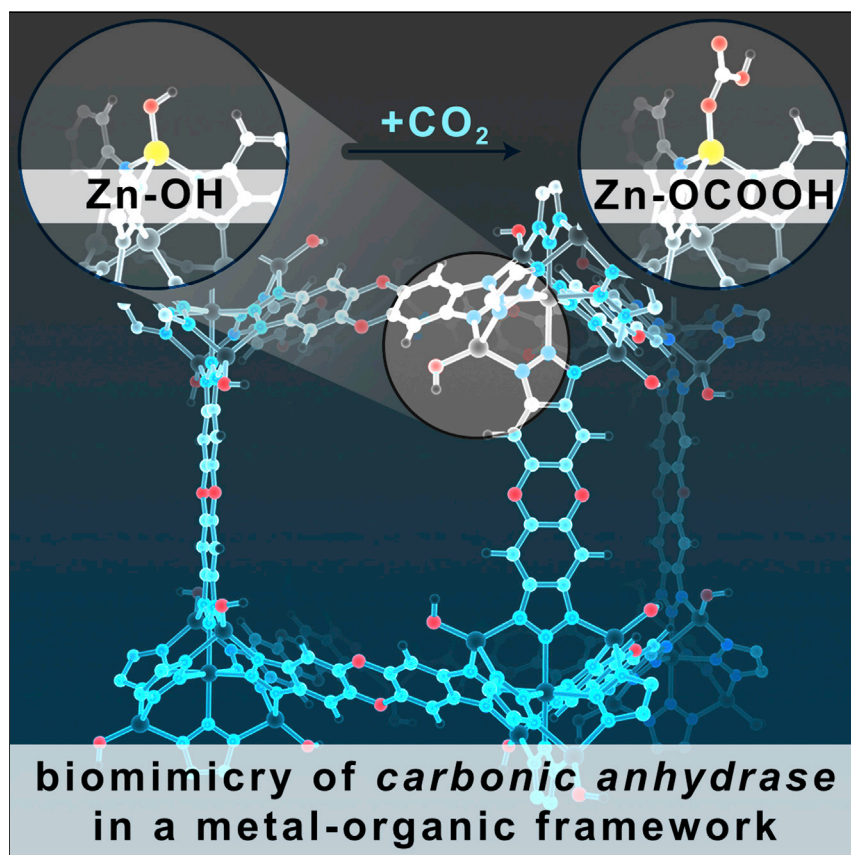**biomimicry of *carbonic anhydrase* in a metal-organic framework**

The nodes of metal-organic frameworks are attractive sites for mimicking metalloenzymes, primarily through their site isolation and similar ligand fields. In this article, the metal-organic framework MFU-4l is shown to mimic the active site of carbonic anhydrase with high structural fidelity and reactivity. The material adsorbs high quantities of carbon dioxide at low pressures and mimics critical features of carbonic anhydrase, such as isotopic exchange of oxygen atoms from water and carbon dioxide.

Ashley M. Wright, Zhenwei Wu, Guanghui Zhang, ..., Christopher H. Hendon, Jeffrey T. Miller, Mircea Dincă

mdinca@mit.edu

HIGHLIGHTS

Hydroxylation of the MFU-4*l* metal node creates a functioning carbonic anhydrase mimic

High uptake volumes of adsorbed carbon dioxide occur at low pressures

Isotopic exchange of ^{18}O from H$_2$O into CO$_2$ is catalyzed by MFU-4*l*-(OH)

7 AFFORDABLE AND CLEAN ENERGY

Chem

CellPress

Article

A Structural Mimic of Carbonic Anhydrase in a Metal-Organic Framework

Ashley M. Wright,[1] Zhenwei Wu,[2] Guanghui Zhang,[2] Jenna L. Mancuso,[3] Robert J. Comito,[1] Robert W. Day,[1] Christopher H. Hendon,[3] Jeffrey T. Miller,[2] and Mircea Dincă[1,4,*]

SUMMARY

Metal-organic frameworks (MOFs) have exciting potential for biomimetic studies of enzymes, yet construction of high-fidelity models at the metal nodes is challenging. Nonetheless, biomimetic MOFs have significant advantages, such as increased stability and ease of separation, over their enzymatic and homogeneous counterparts, making them particularly attractive for industrial applications. Here, we demonstrate biomimetic behavior of Zn hydroxide moieties inside a MOF with structural and reactivity characteristics of carbonic anhydrase. Similar to the biological system, the MOF binds CO_2 by an insertion mechanism into the Zn–OH bond, leading to significant adsorption of CO_2 (3.41 mmol/g). In reactivity mimicking that of the enzyme, the material also catalyzes the oxygen isotope exchange between water and carbon dioxide. Overall, these results provide the strongest evidence yet of metal nodes in MOFs bearing high structural fidelity to enzymatic active sites.

INTRODUCTION

Metal-organic frameworks (MOFs) are promising platforms for biomimetic studies of metalloenzymes.[1–4] The connecting ends of organic linkers in MOFs, such as carboxylates and triazoles, are comparable to the ligands that make up the active sites in metalloenzymes. Consequently, the metal nodes are attractive targets for biomimetic chemistry. The advantages of performing biomimetic chemistry in MOFs over traditional homogeneous systems include (1) site isolation, preventing unwanted bimetallic reactivity and in turn allowing for sterically unhindered metal sites;[5] (2) tunable pore environments, affording hydrophilic or hydrophobic channels, which can mimic the channels found in the enzymes;[3] and (3) higher stability than with enzymes,[6–9] potentially leading to broader use of biomimetic chemistry in industrially relevant applications.

Carbonic anhydrase (CA) is a ubiquitous zinc metalloenzyme that catalyzes the hydration of carbon dioxide. The active site of CA features a divalent zinc in a N_3ZnOH coordination environment, where the zinc exhibits a tetrahedral geometry featuring three histidine groups and a hydroxide (or water) (Figure 1).[10] Much has been learned about CA through modeling the active site with synthetic analogs,[11] such as $Tp^{(tBu,Me)}ZnOH$ (Tp = tris(pyrazolyl)hydroborate), which reacts reversibly with CO_2 and catalyzes oxygen atom exchange between CO_2 and H_2O.[12–14] Accessing similar Tp-like environments within MOFs would afford site-isolated examples of CA. One material whose secondary building units (SBUs) are almost exact structural mimics of the active site in CA is MFU-4l ($Zn_5Cl_4(BTDD)_3$ **1**, where $BTDD^{2-}$ = bis(1,2,3-triazolo[4,5-*b*],[4',5'-*i*])dibenzo[1,4]dioxin) (Figure 1).[15–20] The SBUs, or metal nodes, in this material feature four peripheral zinc chloride sites that are coordinated by three triazoles in C_3 symmetry analogous to the Tp ligand and, accordingly, CA (Figure 1).

The Bigger Picture

Mimicking metalloenzymes at the node of a metal-organic framework (MOF) has the potential to impart enzyme-like catalytic activity within a heterogeneous material. Carbonic anhydrase, one of nature's fastest enzymes, catalyzes the hydrolysis of carbon dioxide into bicarbonate and protons. Notably, carbonic anhydrase mimics have been proposed as potential catalysts for carbon capture and sequestration from the environment. Here, we demonstrate that the metal node of MFU-4*l*, a MOF featuring a metal node with a N_3ZnX coordination environment, can be functionalized to give a mimic of carbonic anhydrase. This work describes a well-defined example of a metal node within a MOF with high structural fidelity to an enzyme active site. It has potential applicability to applications such as CO_2 capture and sequestration and also important gas separations involving CO_2.
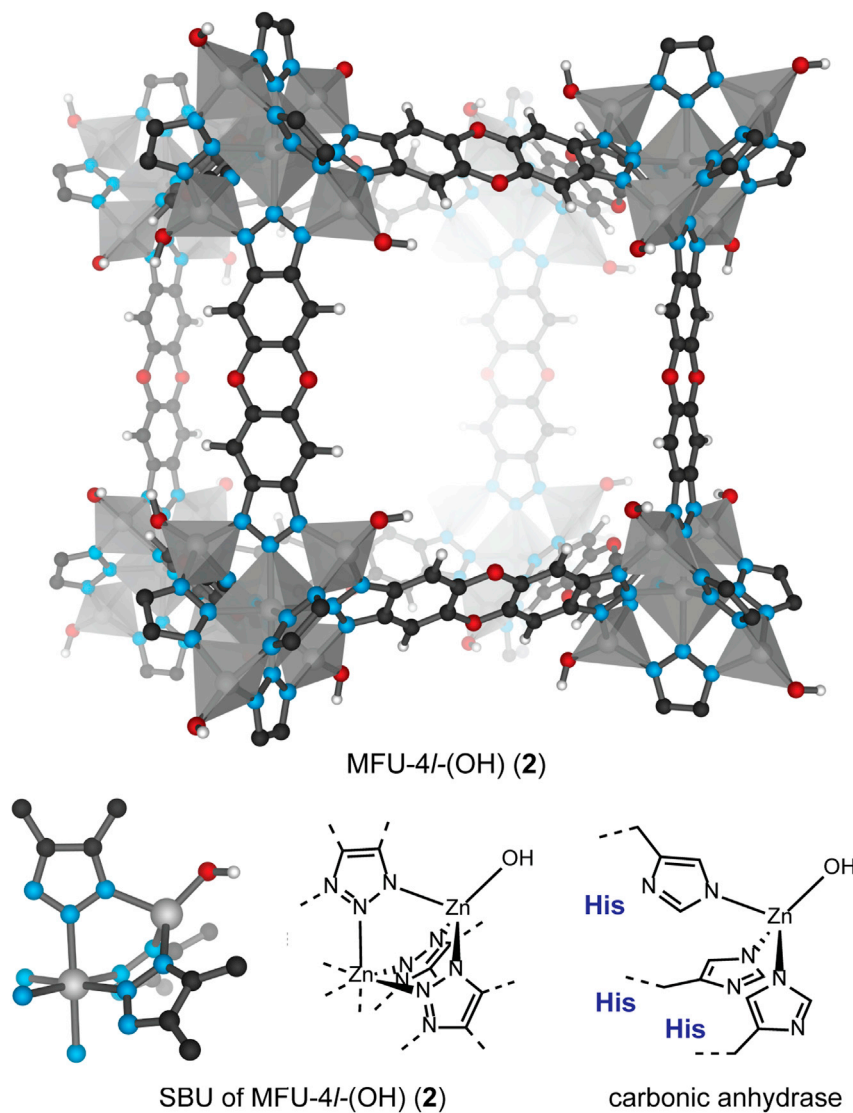
Chem

CellPress

Figure 1. Structure of MFU-4l-(OH) (Top) and Comparison of the Active Site in Carbonic Anhydrase with the Peripheral Zinc in MFU-4l (Bottom)

The structure of MFU-4l-(OH) (**2**) was modeled from the XYZ coordinates of an extended lattice DFT model.

In this article, we demonstrate that the metal node of MFU-4l (**1**) can be modified by anion exchange to create a biomimetic model of CA. The addition of organic hydroxide affords MFU-4l-(OH) (**2**), where original terminal $N_3Zn–Cl$ centers are quantitatively transformed to terminal $N_3Zn–OH$ units. Characterization by X-ray absorption spectroscopy confirms the installation of the hydroxide unit, and subsequent reactivity studies show that **2** reacts with CO_2 and catalyzes oxygen atom exchange between H_2O and CO_2 as well as the hydrolysis of 4-nitrophenyl acetate (4-NPA), consistent with the activity of CA.

RESULTS AND DISCUSSION

Although the terminal chlorides in MFU-4l are known to exchange with a variety of other anions, hydroxide exchange using KOH has been reported to cause decomposition.[21] However, we found that anion metathesis with hydroxide was

[1]Department of Chemistry, Massachusetts Institute of Technology, 77 Massachusetts Avenue, Cambridge, MA 02139, USA

[2]Davidson School of Chemical Engineering, Purdue University, 480 Stadium Mall Drive, West Lafayette, IN 47907, USA

[3]Materials Science Institute, Department of Chemistry and Biochemistry, University of Oregon, Eugene, OR 97403, USA
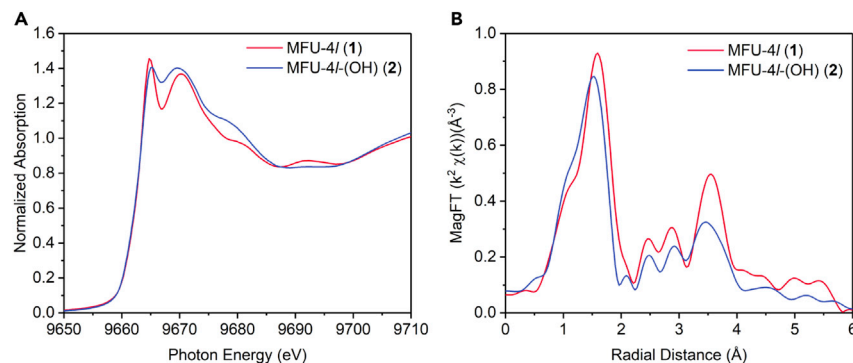
[4]Lead Contact

*Correspondence: mdinca@mit.edu

https://doi.org/10.1016/j.chempr.2018.09.011

Chem

Figure 2. X-Ray Absorption Plots of MFU-4*l* (1) and MFU-4*l*-(OH) (2)
(A) XAS plot of the zinc K-edge XANES spectra for MFU-4*l* (**1**, red trace) and MFU-4*l*-(OH) (**2**, blue trace).
(B) Magnitude of Fourier transform of k^2-weighted EXAFS spectra of MFU-4*l* (**1**, red trace) versus MFU-4*l*-(OH) (**2**, blue trace).

possible through the addition of 10 equiv (2.5 equiv per peripheral zinc) of tetrabutylammonium hydroxide, [TBA][OH], to a suspension of **1** in methanol, which yielded MFU-4*l*-(OH) ($Zn_5(OH)_4(BTDD)_3$, **2**) as a beige microcrystalline solid. Analysis of **2** by powder X-ray diffraction confirmed the retention of crystallinity (Figure S1). Fitting a 77 K N_2 adsorption isotherm of **2** to the Brunauer-Emmett-Teller equation gave a surface area of 2,739 m^2/g, which, although lower than that of **1** (3,525 m^2/g), confirmed the retention of porosity after treatment with base (Figure S2). Thermogravimetric analysis of **2** revealed that it is less stable than its parent **1**; its extrapolated onset decomposition temperature occurs at 250°C, approximately 100°C lower than for **1** (Figure S6). Energy-dispersive X-ray spectroscopy and X-ray photoelectron spectroscopy of **2** confirmed the quantitative replacement of chloride with hydroxide and revealed no chlorine-specific peaks (Figures S4 and S5). Finally, diffuse reflectance infrared Fourier transform spectroscopy (DRIFTS) of **2** revealed a hydroxide O–H stretching band at 3,699 cm^{-1}, a signal that was not observed in the DRIFTS data for **1** (Figure S9). Indeed, the frequency of this band is comparable to that of the OH stretch found in the homologous molecular compound $Tp^{tBu,Me}Zn(OH)$ (3,676 cm^{-1}).[11,12]

To further characterize the incorporation of a Zn–OH site in **2**, we analyzed the material by X-ray absorption spectroscopy (XAS). Whereas both **1** and **2** had the same Zn K-edge energy (9,663.6 eV), indicating a common oxidation state on zinc in both materials (Figure 2A), a significant difference in the zinc coordination environment became apparent when we compared the white line and near-edge regions for the two materials: **2** exhibited a lower and broader white line than **1** and a near-edge feature (~9,668 eV) higher than that of **1** (Figure 2A). Moreover, the extended X-ray absorption fine structure (EXAFS) spectra of **1** and **2** indicated a difference in the primary coordination sphere of zinc. In **2**, the first shell peak shifted to a lower radial distance and was less intense than the corresponding peak in **1** (Figure 2B), consistent with a shorter Zn–X bond and scattering by a lighter element, such as oxygen. Quantitative fitting of the EXAFS region for **2** was challenging because there were two Zn^{2+} sites (N_3ZnX and N_6Zn) with distinct coordination environments, and the small difference between the Zn–N bond length of the two sites made it difficult to fit them as one path or separate paths. Consequently, we chose to fit the difference spectrum of **1** and **2**; the similar coordination environments of the two Zn sites removed the disordered Zn–N scattering in the data, and the fit provided information regarding the Zn–X bond (see Figures S7 and S8 for further details). As a result,
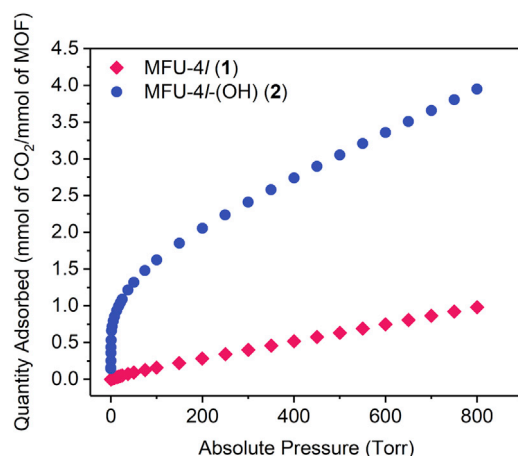
Chem

Figure 3. CO$_2$ Isotherm at 298 K for MFU-4*l* (1; Red Diamonds) and MFU-4*l*-(OH) (2; Blue Circles)

we obtained a satisfactory fit for the Zn–Cl bond distance of 2.17 Å in **1** and for the Zn–O bond distance of 1.93 Å in **2**. For comparison, an extended lattice calculation on **2** (**2-DFT** [density functional theory]) computed a Zn–O bond distance of 1.84 Å (see Supplemental Information), in good agreement with the EXAFS fitting (1.85 Å for comparable molecular analogs) and with CA itself (1.9–2.1 Å).[11]

A critical step in CO$_2$ hydration by CA is CO$_2$ insertion into the Zn–OH bond. After confirming the installation of the Zn–OH group, we probed its reactivity with CO$_2$ by measuring its CO$_2$ adsorption isotherm at 25°C (Figures 3 and S3). Notably, the adsorption isotherm profile featured a significant uptake of CO$_2$ between 0 and 17 Torr, corresponding to 0.86 mmol of CO$_2$ per g of MOF. Importantly, this is equivalent to 1.0 mmol of CO$_2$ per mmol of MOF or the insertion of CO$_2$ into one of four Zn–OH sites in each SBU. The isotherm profile became shallower, and uptake of the remaining ~75% CO$_2$ occurred over a large pressure range of 17–800 Torr. The total CO$_2$ adsorption capacity at 800 Torr was 3.41 mmol/g (4.05 mmol of CO$_2$ per mmol of MOF), which coincides with the total number of Zn–OH sites (3.36 mmol/g) in the MOF. The initial steep uptake supports a strong interaction between **2** and the first CO$_2$ equivalent (per SBU), most likely stemming from the insertion of CO$_2$ into the Zn–OH bond, a unique CO$_2$ capture mechanism that has been observed only once before in a MOF.[22] After the initial steep uptake, the isotherm profile became shallower with increasing coverage, suggesting a change in the interaction between the MOF and CO$_2$ or a shifting of the hydroxide-carbonate equilibrium with increasing CO$_2$ pressure.

To gain more insight into the framework-adsorbate interaction, we determined the coverage-dependent CO$_2$ adsorption enthalpy (Q_{st}) by measuring the CO$_2$ adsorption isotherms at three different temperatures (288, 298, and 308 K) and fitting the isotherm data to the virial equation (Figures S13 and S14).[23,24] Other fitting routines, including the Langmuir, Langmuir-Freundlich, and two-site Langmuir models, provided less satisfactory fits (Figures S11 and S12). With the virial equation, Q_{st} at zero CO$_2$ coverage is 81 kJ/mol, a value much higher than those typically observed in MOFs and other microporous materials[25] and consistent with a chemisorption event. Indeed, the Q_{st} for CO$_2$ insertion into metal–hydroxide bonds in [Mn^{II}Mn^{III}(OH)Cl$_2$(bbta)] and [Co^{II}Co^{III}(OH)Cl$_2$(bbta)] (H$_2$bbta = 1*H*,5*H*-benzo(1,2-d:4,5-d)bistriazole) is 99 and 110 kJ/mol, respectively.[22] Notably, the coverage-dependent Q_s suggests a bimodal adsorption profile (Figure S15). With increasing
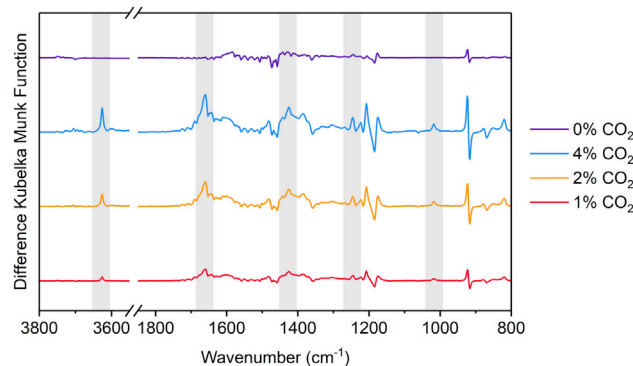
Chem

Figure 4. Difference DRIFTS Plots Collected on MFU-4l-(OH) (2) with Increasing Concentrations of CO₂ in an Argon Carrier Gas

The shaded areas denote new bands assigned to vibrations of a bicarbonate ligand (HCO_3^-). The purple trace (0% CO_2) was collected after the blue trace (4% CO_2).

coverage, Q_{st} stays relatively constant up to ~0.5 equiv of CO_2 per SBU and then gradually decreases until it reaches ranges between 62 and 35 kJ/mol for the second CO_2 equivalent and between 35 and 20 kJ/mol for the third CO_2 equivalent. The large, bimodal variation in Q_{st} suggests that the adsorption mechanism changes with increasing CO_2 coverage.

We modeled CO_2 insertion into the Zn–OH bond by using DFT (PBE/6-311G**). To do so, we used a truncated model of the SBU, $Zn_5(OH)_4(BTA)_6$ (BTA = benzotriazole). Optimization of the cluster model gave a Zn–O(H) bond distance of 1.85 Å and Zn–N bond distances of 2.02–2.05 Å, consistent with the EXAFS fit and extended lattice DFT model. Notably, although the calculated enthalpy of CO_2 insertion into the first Zn–OH unit was −50 kJ/mol, the second, third, and fourth CO_2 molecules were calculated to bind, also by insertion into Zn–OH units, with a lower energy of approximately −44 kJ/mol. The trend of decreasing binding enthalpy is also in qualitative agreement with the experimental data. We postulate that the conversion of the highly basic –OH to weakly basic –OCO_2H perturbs the coordination environment of the SBU enough to weaken the nucleophilicity of the remaining three Zn–OH sites within a given metal node. Given that the nucleophilic strength of Zn–OH correlates with its reactivity toward CO_2,[26] less nucleophilic Zn–OH units shift the Zn–OH + CO_2 ⇌ Zn–OCO_2H equilibrium to the left. A comparable trend of initially high heat of adsorption to lower heat of adsorption was observed in $[M^{II}M^{III}(OH)Cl_2(bbta)]$.[22]

To determine the nature of the chemisorption interaction, we monitored the reaction between **2** and CO_2 by DRIFTS. Exposing **2** to incremental increases in $[CO_2]$ from 1,000 to 4,000 ppm in an argon carrier gas resulted in the formation of new bands in the DRIFT spectrum (Figure 4). By contrast, the addition of CO_2 to **1** under the same conditions resulted in no spectral changes (Figures S22 and S23). The new spectral features in **2** are consistent with the formation of a zinc bicarbonate, which is also the product of CO_2 insertion in CA. Specifically, a new band at 3,626 cm^{-1} was assigned to the O–H stretch.[13] Bands at 1,660 and 1,245 cm^{-1} corresponded to the O=C–O asymmetric and symmetric stretches, respectively.[13] Additionally, bands at 1,018 and 1,423 cm^{-1} were associated with bending and stretching vibrations of the COH group in bicarbonate. The observed stretches were comparable to those of the molecular analog $^{tBu,Me}TpZn(OCO_2H)$, which featured asymmetric and symmetric O=C–O stretches at 1,675 and 1,302 cm^{-1}, respectively.[13] In addition, the IR

Chem

spectrum of $[Mn^{II}M^{III}(OCO_2H)Cl_2(bbta)]$ (M = Mn, Co) featured stretches at 3,682 (O–H), 1,224 (symmetric O–C=O), and 1,050 cm^{-1} (O–H bending).[22] Purging the DRIFTS setup with 100% argon flow resulted in the loss of the new signals and reformation of the starting spectrum, consistent with a reversible reaction with CO_2.

We further illustrated the critical role of the hydroxide ligand in CO_2 uptake by comparing the CO_2 sorption properties of **1** and **2**. MOF **1**, containing a Zn–Cl bond and a saturated metal center, showed a CO_2 adsorption capacity at 800 Torr of 0.98 mmol of CO_2/mmol of MOF (1.23 mmol of CO_2 per g of MOF), which is approximately four times smaller than the overall capacity of **2** (Figure 3). The zero-coverage Q_{st}, 20 kJ/mol, was also significantly lower than the Q_{st} of **2** (Figures S16–S19). Most notably, at 17 Torr, **2** adsorbed 0.99 mmol of CO_2 per mmol of MOF, which is approximately 300 times more CO_2 than **1** (0.0031 mmol of CO_2 per mmol of MOF) at the same pressure. The large uptake at low pressures demonstrates the potential utility of CO_2 insertion into the M–OH bond for CO_2 sorption applications.

Next, we investigated the ability of **1** and **2** to perform CA-like reactivity. The central function of CA is to rapidly interconvert H_2O and CO_2 as well as bicarbonate and protons. We mimicked the interconversion *in vitro* by studying the exchange of ^{18}O-labeled H_2O with gaseous CO_2 and periodically sampling the headspace to monitor the distribution of CO_2 isotopologues by gas chromatography-mass spectroscopy. Notably, in the presence of **2**, the time to reach an equilibrium mixture of the three possible CO_2 isotopologues ($C^{16}O_2$, $C^{16,18}O_2$, and $C^{18}O_2$) was significantly reduced to 5 hr from 10 hr without **2** (Figures S28–S31). Consequently, there must be a rapid equilibrium for the Zn–OH + CO_2 $\rightleftharpoons$ Zn–OCO_2H and Zn–OCO_2H + H_2O $\rightleftharpoons$ Zn–OH + H_2CO_3 reactions. It should be noted that **1** also decreased the time taken to reach an equilibrium mixture of the isotopologues but was not as effective as **2** because it reduced the equilibrium time to 7 hr. This could be attributed to partial hydrolysis of the Zn–Cl bond under the reaction conditions.

A second CA-like reaction often mimicked *in vitro* is the hydrolytic cleavage of 4-NPA. For instance, Jin and co-workers reported that the MOF CFA-1 ($Zn_5(OAc)_4$ (bibta)$_3$, where bibta^{2-} = 5,5′-bibenzo[d][1,2,3]triazole, **CFA-1**)[27] replicated the chemistry of CA through hydration of CO_2 and hydrolysis of 4-NPA.[28] Using similar reactivity conditions, we compared **1**, **2**, and **CFA-1** for their activity in the hydrolysis of 4-NPA (Figures S32–S34). The reactions were performed with ∼2.5 mol % (10 mol % per Zn–X) MFU-4*l* (**1**) and MFU-4*l*-(OH) (**2**) in 50 mM HEPES buffer solution. They were sampled after 3, 6, 24, and 48 hr and were monitored by UV-vis spectroscopy for the formation of 4-nitrophenol (405 nm). A control reaction revealed small (1.7% ± 0.2%) conversion of 4-NPA after 24 hr in the absence of a MOF. Adding **1**, **2**, or **CFA-1** to the reaction mixture increased the conversion yield to 11% ± 2%, 15% ± 2%, and 14% ± 2%, respectively, at the 24 hr time point. In the conversion to mmol of product per mmol of Zn–X sites, this corresponds to low values of 1.2 ± 2, 1.8 ± 2, and 1.0 ± 1 for **1**, **2**, and **CFA-1**, respectively (Table S5). MFU-4*l*-(OH) **2** outperformed both **1** and **CFA-1**, most likely because **1** and **CFA-1** need to undergo ligand exchange to generate the Zn–OH active site. The low turnover number could be caused by pore blocking or slow diffusion through the micropores. Critically, this demonstrates that the N_3ZnOH coordination environment in **2** is a functional mimic of the CA reactivity.

In summary, we have demonstrated that the metal nodes of MFU-4*l* can be functionalized to create a high-fidelity biomimetic model of the CA active site. Reactions

Chem

performed by the enzymes, such as CO_2 insertion into the Zn–OH groups of the metal nodes and hydrolysis of 4-NPA, are mimicked in the MOF. These results demonstrate a rare example of functionalizing a MOF metal node to mimic the activity of an enzyme. The nascent field of biomimetic chemistry in MOFs holds potential for future understanding of enzyme chemistry and also the potential to perform enzyme-inspired reactions in stable frameworks. For instance, the insertion of CO_2 into a metal-hydroxide bond could lead to CO_2 separations with limited energy cost in regeneration, a concept we are currently exploring through implementing the chemistry of **2** in membrane composites for gas separations.

SUPPLEMENTAL INFORMATION

Supplemental Information includes Supplemental Experimental Procedures, 36 figures, and 8 tables and can be found with this article online at https://doi.org/10.1016/j.chempr.2018.09.011.

AUTHOR CONTRIBUTIONS

A.M.W. and M.D. conceptualized the experiments. A.M.W. synthesized materials and performed experiments. Z.W., G.Z., R.J.C., and J.T.M. collected and analyzed X-ray absorption spectroscopy data. R.W.D. and A.M.W. collected and analyzed X-ray photoelectron spectroscopy and energy-dispersive X-ray spectroscopy data. J.L.M. and C.H.H. performed computational studies. A.M.W. and M.D. wrote the original manuscript. All authors proofread, commented on, and approved the final manuscript for submission.

DECLARATION OF INTERESTS

The authors declare no competing interests.

REFERENCES AND NOTES

1. Nath, I., Chakraborty, J., and Verpoort, F. (2016). Metal organic frameworks mimicking natural enzymes: a structural and functional analogy. Chem. Soc. Rev. *45*, 4127–4170.

2. Chen, Y., and Ma, S. (2016). Biomimetic catalysis of metal-organic frameworks. Dalton Trans. *45*, 9744–9753.

3. Chen, K., and Wu, C.-D. (2018). Designed fabrication of biomimetic metal–organic frameworks for catalytic applications. Coord. Chem. Rev. Published online February 13, 2018. https://doi.org/10.1016/j.ccr.2018.01.016.

4. Zhao, M., Ou, S., and Wu, C.-D. (2014). Porous metal-organic frameworks for heterogeneous biomimetic catalysis. Acc. Chem. Res. *47*, 1199–1207.

5. Gu, Z.Y., Park, J., Raiff, A., Wei, Z., and Zhou, H.C. (2014). Metal-organic frameworks as biomimetic catalysts. ChemCatChem *6*, 67–75.

6. Lykourinou, V., Chen, Y., Wang, X.S., Meng, L., Hoang, T., Ming, L.J., Musselman, R.L., and Ma, S. (2011). Immobilization of MP-11 into a mesoporous metal-organic framework, MP-11@mesoMOF: a new platform for enzymatic catalysis. J. Am. Chem. Soc. *133*, 10382–10385.

7. Li, P., Modica, J.A., Howarth, A.J., Vargas, L.E., Moghadam, P.Z., Snurr, R.Q., Mrksich, M., Hupp, J.T., and Farha, O.K. (2016). Toward design rules for enzyme immobilization in hierarchical mesoporous metal-organic frameworks. Chem *1*, 154–169.

8. Mehta, J., Bhardwaj, N., Bhardwaj, S.K., Kim, K.-H., and Deep, A. (2016). Recent advances in enzyme immobilization techniques: metal-organic frameworks as novel substrates. Coord. Chem. Rev. *322*, 30–40.

9. Li, P., Moon, S.Y., Guelta, M.A., Lin, L., Gómez-Gualdrón, D.A., Snurr, R.Q., Harvey, S.P., Hupp, J.T., and Farha, O.K. (2016). Nanosizing a metal-organic framework enzyme carrier for accelerating nerve agent hydrolysis. ACS Nano *10*, 9174–9182.

10. Liang, J.Y., and Lipscomb, W.N. (1990). Binding of substrate CO_2 to the active site of human carbonic anhydrase II: a molecular dynamics study. Proc. Natl. Acad. Sci. USA *87*, 3675–3679.

11. Parkin, G. (2004). Synthetic analogues relevant to the structure and function of zinc enzymes. Chem. Rev. *104*, 699–767.

Chem

CellPress

12. Alsfasser, R., Vahrenkamp, H., Trofimenko, S., Looney, A., and Parkin, G. (1991). A mononuclear zinc hydroxide complex stabilized by a highly substituted tris(pyrazolyl) hydroborato ligand: analogies with the enzyme carbonic anhydrase. Inorg. Chem. 30, 4098–4100.

13. Looney, A., Parkin, G., Alsfasser, R., Ruf, M., and Vahrenkamp, H. (1992). Zinc pyrazolylborate complexes relevant to the biological function of carbonic anhydrase. Angew. Chem. Int. Ed. 31, 92–93.

14. Looney, A., Han, R., McNeill, K., and Parkin, G. (1993). Tris(pyrazolyl)hydroboratozinc hydroxide complexes as functional models for carbonic anhydrase: on the nature of the bicarbonate intermediate. J. Am. Chem. Soc. 115, 4690–4697.

15. Biswas, S., Grzywa, M., Nayek, H.P., Dehnen, S., Senkovska, I., Kaskel, S., and Volkmer, D. (2009). A cubic coordination framework constructed from benzobistriazolate ligands and zinc ions having selective gas sorption properties. Dalton Trans. 6487–6495.

16. Denysenko, D., Werner, T., Grzywa, M., Puls, A., Hagen, V., Eickerling, G., Jelic, J., Reuter, K., and Volkmer, D. (2012). Reversible gas-phase redox processes catalyzed by co-exchanged MFU-4l(arge). Chem. Commun. (Camb.) 48, 1236–1238.

17. Comito, R.J., Fritzsching, K.J., Sundell, B.J., Schmidt-Rohr, K., and Dincă, M. (2016). Single-site heterogeneous catalysts for olefin polymerization enabled by cation exchange in a metal-organic framework. J. Am. Chem. Soc. 138, 10232–10237.

18. Denysenko, D., Grzywa, M., Jelic, J., Reuter, K., and Volkmer, D. (2014). Scorpionate-type coordination in MFU-4l metal-organic frameworks: small-molecule binding and activation upon the thermally activated formation of open metal sites. Angew. Chem. Int. Ed. 53, 5832–5836.

19. Dubey, R.J., Comito, R.J., Wu, Z., Zhang, G., Rieth, A.J., Hendon, C.H., Miller, J.T., and Dincă, M. (2017). Highly stereoselective heterogeneous diene polymerization by Co-MFU-4l: a single-site catalyst prepared by cation exchange. J. Am. Chem. Soc. 139, 12664–12669.

20. Wright, A.M., Rieth, A.J., Yang, S., Wang, E.N., and Dincă, M. (2018). Precise control of pore hydrophilicity enabled by post-synthetic cation exchange in metal-organic frameworks. Chem. Sci. (Camb.) 9, 3856–3859.

21. Denysenko, D., Jelic, J., Reuter, K., and Volkmer, D. (2015). Postsynthetic metal and ligand exchange in MFU-4l: a screening approach toward functional metal-organic frameworks comprising single-site active centers. Chemistry 21, 8188–8199.

22. Liao, P.-Q., Chen, H., Zhou, D.-D., Liu, S.-Y., He, C.-T., Rui, Z., Ji, H., Zhang, J.-P., and Chen, X.-M. (2015). Monodentate hydroxide as a super strong yet reversible active site for CO_2 capture from high-humidity flue gas. Energy Environ. Sci. 8, 1011–1016.

23. Czepirski, L., and Jagiełło, J. (1989). Virial-type thermal equation of gas-solid adsorption. Chem. Eng. Sci. 44, 797–801.

24. Dincă, M., Dailly, A., Liu, Y., Brown, C.M., Neumann, D.A., and Long, J.R. (2006). Hydrogen storage in a microporous metal-organic framework with exposed Mn2+ coordination sites. J. Am. Chem. Soc. 128, 16876–16883.

25. Sumida, K., Rogow, D.L., Mason, J.A., McDonald, T.M., Bloch, E.D., Herm, Z.R., Bae, T.H., and Long, J.R. (2012). Carbon dioxide capture in metal-organic frameworks. Chem. Rev. 112, 724–781.

26. Bräuer, M., Pérez-Lustres, J.L., Weston, J., and Anders, E. (2002). Quantitative reactivity model for the hydration of carbon dioxide by biomimetic zinc complexes. Inorg. Chem. 41, 1454–1463.

27. Schmieder, P., Denysenko, D., Grzywa, M., Baumgärtner, B., Senkovska, I., Kaskel, S., Sastre, G., van Wüllen, L., and Volkmer, D. (2013). CFA-1: the first chiral metal-organic framework containing Kuratowski-type secondary building units. Dalton Trans. 42, 10786–10797.

28. Jin, C., Zhang, S., Zhang, Z., and Chen, Y. (2018). Mimic carbonic anhydrase using metal-organic frameworks for CO_2 capture and conversion. Inorg. Chem. 57, 2169–2174.

Supplemental Information

A Structural Mimic of Carbonic Anhydrase

in a Metal-Organic Framework

Ashley M. Wright, Zhenwei Wu, Guanghui Zhang, Jenna L. Mancuso, Robert J. Comito, Robert W. Day, Christopher H. Hendon, Jeffrey T. Miller, and Mircea Dincă

Table of Contents

General Procedures

Materials

$ZnCl_2 \cdot 6H_2O$ (99.9%, Alfa Aesar), HCl (32-35%, BDH – VWR Analytic) methanol (99.9%, VWR), *N,N*-dimethylformamide (DMF, 99.8%, Millipore), ethanol (ACS grade, Mallinckrodt), tetra-*n*-butylammonium hydroxide (1.5 M, water, Sigma Aldrich) were used as received. MFU-4*l* was synthesized using previously published procedures.[1]

Powder X-ray Diffraction (PXRD) patterns were recorded with a Bruker Advance II diffractometer equipped with a θ/2θ Bragg-Brentano geometry and Ni-filtered CuKα radiation (Kα$_1$ = 1.5406 Å, Kα$_2$ = 1.5444 Å, Kα$_1$/ Kα$_2$ = 0.5). The tube voltage and current were 40 kV and 40 mA, respectively. Samples for PXRD were prepared by placing a thin layer of the appropriate material on a zero-background silicon crystal plate.

Gas adsorption isotherms were measured by a volumetric method using a Micromeritics ASAP 2020 gas sorption analyzer. Typical samples of ca. 40–80 mg, preactivated at >100°C to remove all residual solvent, were transferred in an Ar-filled glovebox to a pre-weighed analysis tube. The tube with sample inside was weighed again to determine the mass of the sample. The tube was capped with a Micromeritics TranSeal™, brought out of the glovebox, and transferred to the analysis port of the gas sorption analyzer. Free space correction measurements were performed using ultra-high purity He gas (UHP grade 5, 99.999% pure). Nitrogen isotherms were measured using UHP grade Nitrogen. All nitrogen analyses were performed using a liquid nitrogen bath at 77 K. Carbon dioxide isotherms were measured using Research grade carbon dioxide (99.999%). Carbon dioxide analyses were performed at varying temperatures in a water/ethylene glycol isothermal bath. Oil-free vacuum pumps were used to prevent contamination of sample or feed gases.

Thermogravimetric Analysis (TGA) was performed on a TA Instruments Q500 Thermogravimetric Analyzer at a heating rate of 2 °C/min under a nitrogen gas flow of 10 mL/min.

Diffuse reflectance infrared Fourier transform spectroscopy (DRIFTS) measurements were performed on a Bruker Tensor 37 with a mercury cadmium telluride detector cooled to 77 K. Data were collected in "MIR_DRIFTS" mode with a 6mm aperture setting and a KBr beam splitter using a DiffusIR accessory made by Pike Technologies in an in-situ cell equipped with a ZnSe window. Data was averaged over 32 scans between 4000 and 600 cm^{-1}. Samples were diluted with KBr to ~5% by weight and loaded in to ceramic sample cup. A background of KBr was subtracted from the data.

Synthesis of MFU-4*l*-(OH) (2).

tetrabutylammonium hydroxide (2.7 mL, 4.1 mmol, 20 equiv.) was added dropwise to a gently stirring suspension of MFU-4*l* (**1**) (255 mg, 0.202 mmol) in methanol under a nitrogen atmosphere. The mixture was slowly stirred for 18 hours, then the solid was isolated on a medium porosity frit in air. The solid was washed with MeOH (12 × 30 mL portions) over 48 hours to remove [TBA][Cl] and excess [TBA][OH]. The solid was dried under vacuum at 110 °C for 18 hours and stored in an argon glove box prior to use. Amount isolated: 200 mg, 85% yield.

Powder X-ray Diffraction
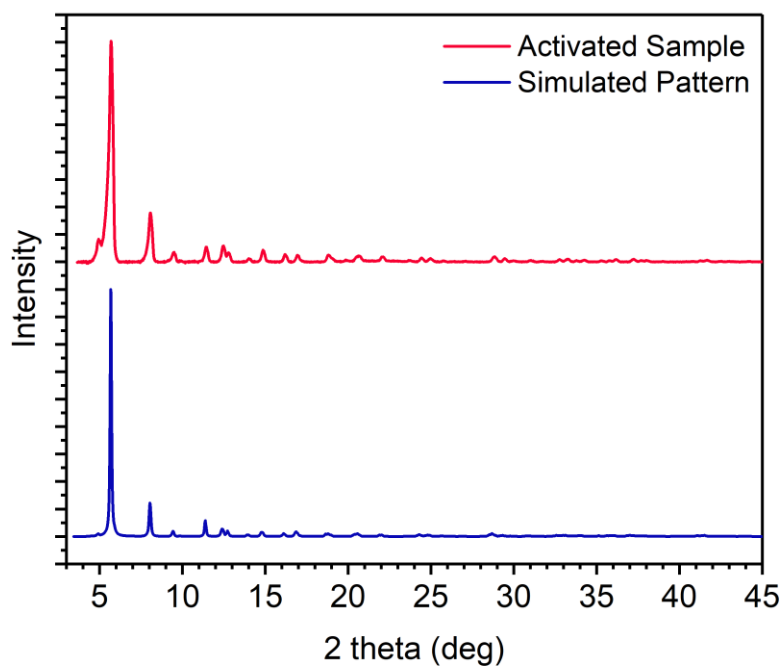
Figure S1. Powder X-ray diffraction pattern of an activated sample of MFU-4*l*-(OH) (**2**) (top trace, red) and the simulated pattern of MFU-4*l*-(OH) (**2**) (bottom trace, blue) as determined from the DFT extended lattice model.

Gas adsorption isotherms
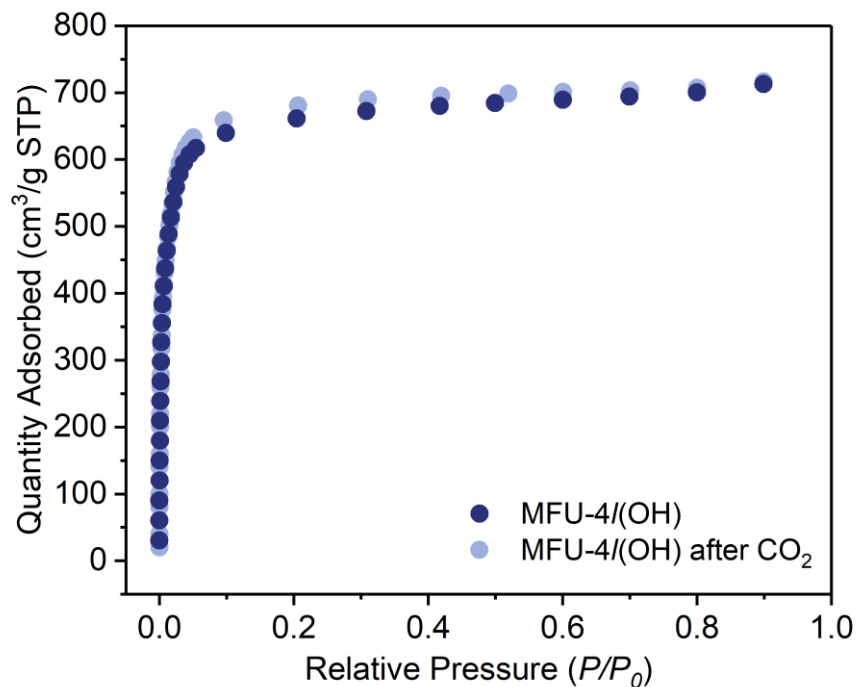
Figure S2. N_2 adsorption isotherm at 77 K before (blue circles) and after exposure to CO_2 (light blue circles). BET surface areas: before, 2739 m^2/g; after 2875 m^2/g.

Table S1. BET parameters and pressure ranges used for the calculation of the BET surface area for MFU-4*l*-(OH).

Material	MFU-4*l*-(OH) before CO_2	MFU-4*l*-(OH) after CO_2
BET surface area	2739 m^2/g	2875 m^2/g
P/P_0 range	0.009 – 0.055	0.009 – 0.051
C	244.4	206.2
V_m	629 m^2/g	661 m^2/g
P/P_0 (@ V_m)	0.07	0.096
$1/(\sqrt{C}+1)$	0.060	0.065
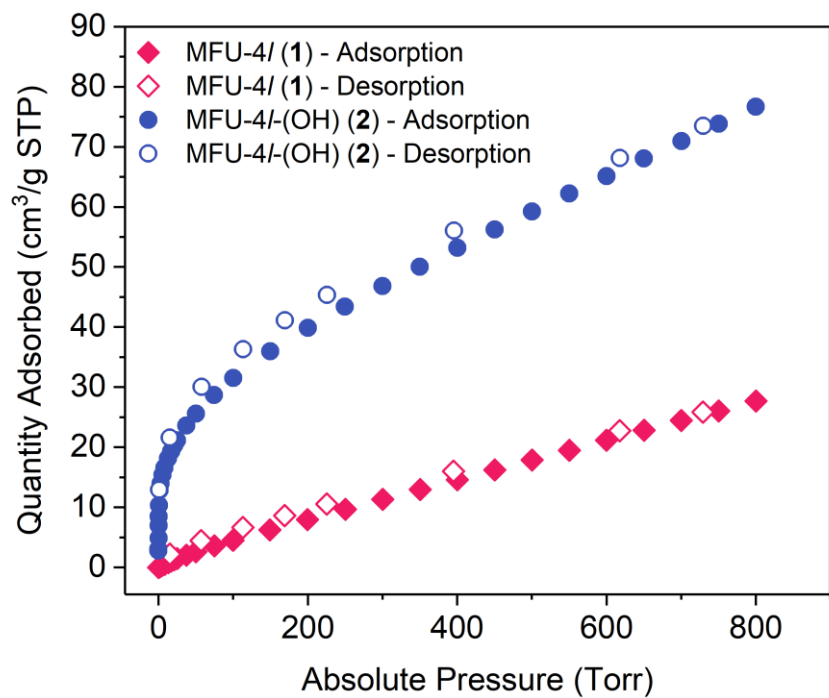
Figure S3. Comparison of the CO_2 adsorption isotherms of MFU-4*l*-(OH) (**2**) (blue circles) and MFU-4*l* (**1**) (red diamonds) at 298 K. The closed symbols denote the adsorption phase and the open symbols represent the desorption phase.

X-ray Photoelectron Spectroscopy
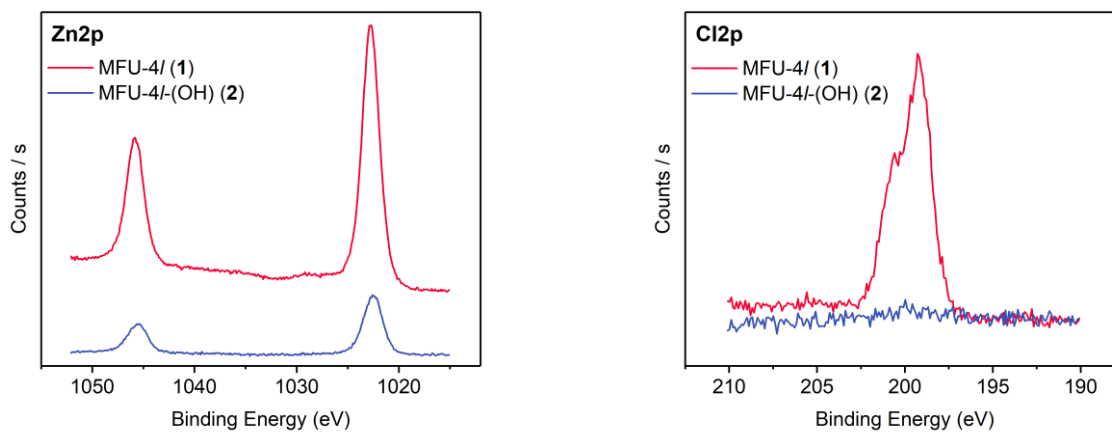
Figure S4. High resolution XPS spectra of MFU-4*l* (**1**, red line) and MFU-4*l*-(OH) (**2**, blue line) in the Zn2p and Cl2p regions. The lack of signal in the Cl2p region for **2** is consistent with no chloride present.
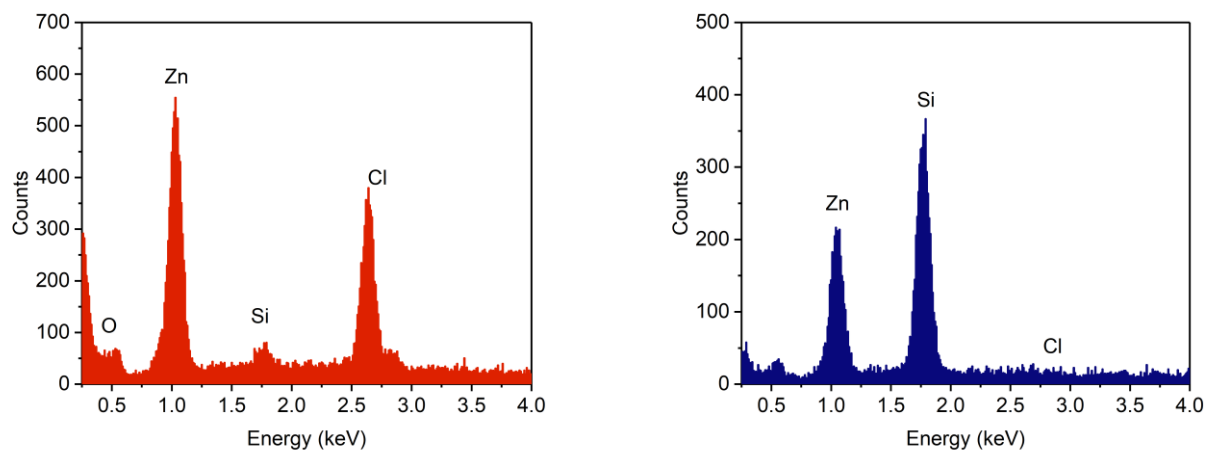
Figure S5. Energy-dispersive X-ray spectroscopy of MFU-4*l* (**1**) (left, red) and MFU-4*l*-(OH) (**2**) (right, blue). The EDXS spectrum of **2** indicates no chloride in the bulk sample supporting exchange of OH for Cl. The Si signal is from the substrate material.
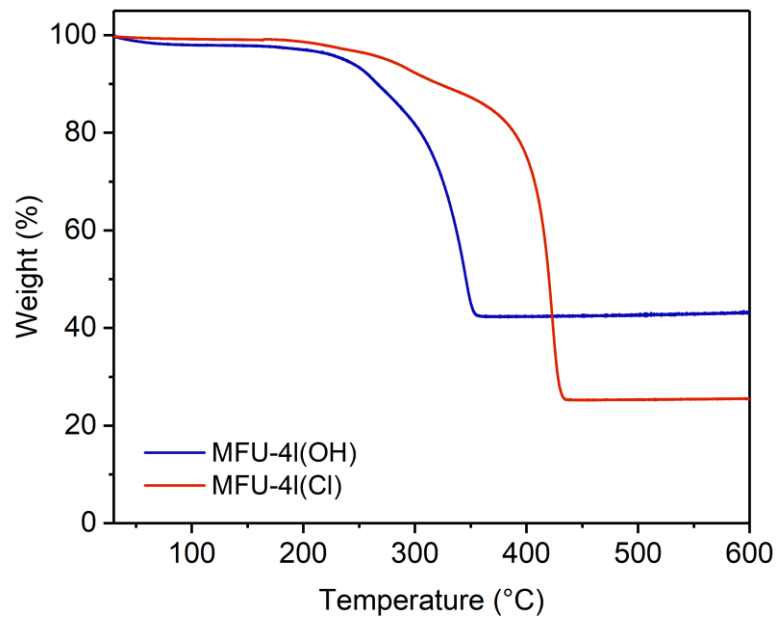
Figure S6. Thermogravimetric analysis (TGA) curves for MFU-4*l* (**1**, red) and MFU-4*l*-(OH) (**2**, blue).

X-ray Absorption Spectroscopy (XAS) Analysis of MFU-4*l*-(OH) and MFU-4*l*

X-ray absorption spectroscopy measurements at the Zn K edge (9658.6 eV) were performed on the 10-ID line of the Materials Research Collaborative Access Team (MRCAT) at the Advanced Photo Source (APS), Argonne National Laboratory.

Below are the XANES plot of MFU-4*l* (**1**) and MFU-4*l*-(OH) (**2**) (**Figure S7**). Both samples have the same edge energy of 9663.6 eV characteristic of Zn(II). The whiteline and near edge features, however, are different between the two samples. The MFU-4*l*-(OH) has slightly lower and broader whiteline compared to MFU-4*l*. The near edge feature after whiteline is higher, which is evident of changes in the coordination environment around Zn. More information is obtained from the EXAFS spectra (**Figure S8**). Compared to MFU-4*l*, the first shell EXAFS peak of MFU-4*l*-(OH) sample shift to lower radial distance, which corresponds to a shorter average bond distance and is consistent with the proposed ligand replacement of Cl by OH. In addition, the first shell peak of MFU-4*l*-(OH) sample decreases slightly in intensity, again consistent with oxygen being a lighter scatter compared to Cl.
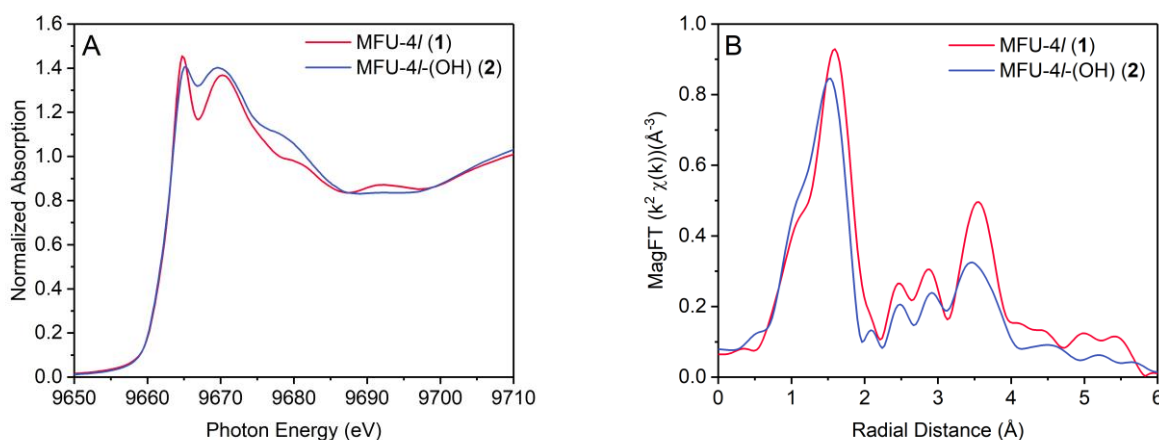
Figure S7. (A) XANES plot of the zinc K-edge for MFU-4*l* (red trace) and MFU-4*l*(OH) (blue trace). (B) Magnitude of Fourier transform of k^2 weighted EXAFS spectra of MFU-4*l* (**1**) vs MFU-4*l*-OH (**2**).

Quantitative EXAFS fitting.

To directly examine the coordination environment around Zn and obtain quantitative information, we turn to EXAFS fitting. In a typical fitting approach, we examine the EXAFS data of a certain sample and how close it is to the simulation from a proposed structure model. Briefly, an initial bond length and coordination number from certain structure model is used in the fits and fitting the data gives the amplitude reduction factor S_0^2, energy shift ΔE_0, bond distance difference ΔR and Debye-Waller factor σ^2 values, which are all reflective of whether the

model is physically close to the real sample. A good fit is obtained by adjusting the model (coordination number as well as bond distances) until reasonable S_0^2, ΔE_0, ΔR and σ^2 values are obtained.

For this sample, direct fitting of the EXAFS data of a certain sample is very challenging due to the presence of two types of Zn with distinct coordination environments (central Zn in an N_6Zn environment and peripheral Zn in a N_3ZnX environment). These two types of Zn have Zn—N bonds in two sets of different distances, but the bond distances do not differ significantly, making it hard to fit them as either one path or separate paths. Alternatively, we take the difference between the EXAFS ($\chi(k)$) of MFU-4l and MFU-4l-OH and fit the difference spectrum (**Figure S8A**). Due to the presumably similar overall Zn coordination environment between the two samples, taking this difference should, at best if not totally, remove the same multiple Zn—N scatterings in the data. According to the proposed sample structure, this difference EXAFS represents the coordination change due to the anion exchange, corresponding to 0.8 Zn—Cl scattering plus – 0.8 Zn—O scattering. The coordination number is 0.8 instead of 1 since the one Zn—X coordination change on each four peripheral Zn is averaged to all five Zn in each SBU in EXAFS which is a bulk average technique. The "negative" Zn—O scattering is due to the data subtraction and equivalent to a Zn—O scattering with inverse phase shift and can be simulated and fit in the Artemis software.[1] **Figure S8b** shows the imaginary part of the fit summing an inverse Zn-O path and a Zn-Cl path.
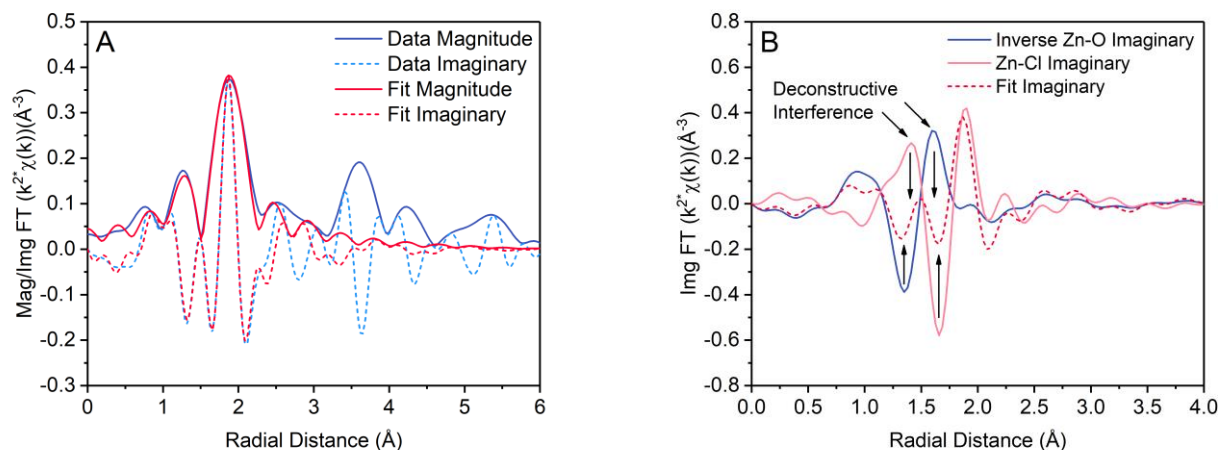

Figure S8. (A) Fitting results (red) of the difference EXAFS spectra between MFU-4l and MFU-4l-OH (blue), the plots show the magnitude (solid) and imaginary part (dash) of the Fourier transform of k^2 weighted EXAFS, k: 2.7 – 10.0 Å^{-1}, R: 1.0 - 2.3 Å; (B) Comparison between the summed imaginary part with that of the Zn—O and Zn—Cl scattering path. The two different paths happen to show strong deconstructive interference between 1.1 Å and 1.7 Å.

The approach of fitting of the difference spectrum resulted in a satisfactory fit of Zn—Cl bond of 2.17 Å and Zn—O bond of 1.93 Å, with an amplitude reduction factor of 0.93. The obtained Zn—Cl bond distance is very similar to the calculated bond distance for MFU-4*l* as well as the Ni—Cl and Co—Cl bond distances obtained from previous EXAFS fitting of the Ni and Co-MFU-4*l* samples (~2.15 Å). The Zn—O bond distance is longer than the value from DFT calculation but is within the reasonable range for Zn—O bonds in tetrahedral geometry. For instance, ZnO has tetrahedral Zn—O bonds of 1.97 Å. Other common compounds of late 3d transitional metals in tetrahedral geometry also feature O bonds in a distance between 1.9 and 2.0 Å. The amplitude reduction factor S_0^2 in the fit is also close to the value obtained from ZnO reference (0.97), confirming that this is a physically reasonable fit. In addition, the fit well explains the dip at around 1.5 Å (phase uncorrected distance) in the magnitude of k^2 weighted difference EXAFS (**Figure S8a**). This feature comes from a strong deconstructive interference between Zn—Cl and inverse phase Zn—O scattering as shown in **Figure S8b**. The fit is also consistent with varied data range in k and R space of the data.

Overall, both qualitative and quantitative analysis of the XAS data verifies that in the MFU-4*l*-(OH) sample, the original Cl ligand attached to the Zn in the ion exchange site of MFU-4l has been replaced by OH ligand.

Table S2. Fitting results for the difference EXAFS between MFU-4*l* (**1**) and MFU-4*l*-(OH) (**2**) and ZnO reference.

Sample	Scattering Pair	S_0^2 *	CN	Bond Length (Å) *	ΔE_0 (eV) *	σ^2 (Å ^{2}) *
ZnO	Zn—O	0.97	4	1.97	3.0	0.005
MFU-4*l* – MFU-4*l*-OH	Zn—Cl	0.93	0.8	2.17	1.6	0.004
	Zn—O		0.8	1.93		0.005

* The average error in S_0^2 is 0.2, in bond length is 0.02 Å, in ΔE_0 is 2.0 eV and in $\Delta\sigma^2$ is 0.002 Å.
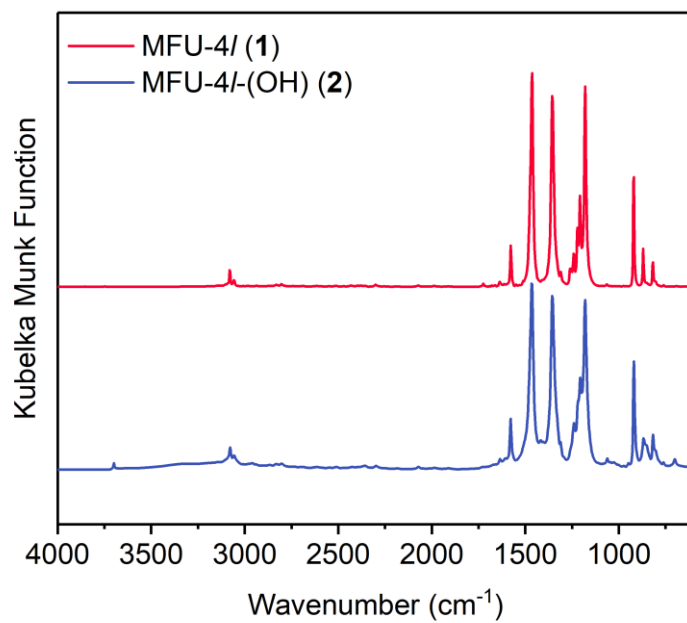
IR spectroscopy

Figure S9. DRIFT spectrum of MFU-4*l* (**1**) (top, red trace) and MFU-4*l*-(OH) (**2**) (bottom, blue trace).
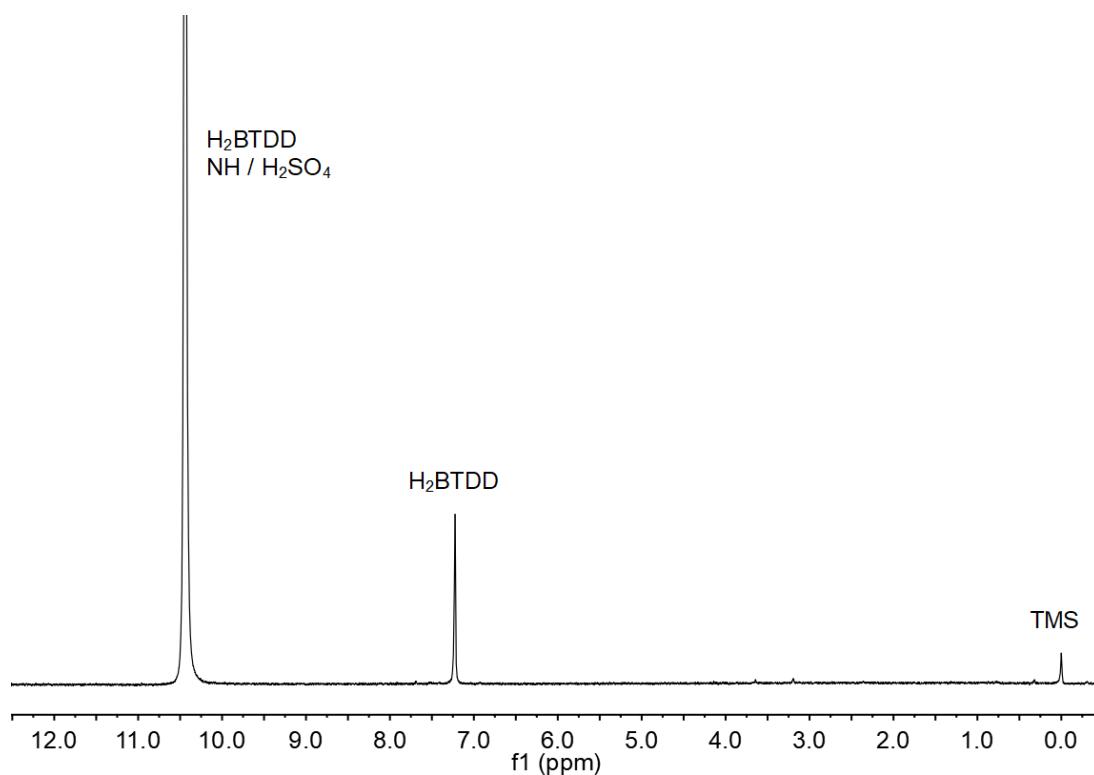
Digestion of MFU-4*l*-(OH) in D₂SO₄

Figure S10. ¹H NMR spectrum (D₂SO₄, 300 MHz) of MFU-4*l*-(OH) (~3.5 mg) digested in D₂SO₄. The ¹H NMR spectrum shows the presence of the ligand in the digested sample. No signals corresponding to the ⁿBu₄N⁺ cation was observed in the spectrum revealing the cation does not remain in the MOF after anion exchange.

Isosteric Heats of Adsorption Calculations

To determine the isosteric heat of adsorption (Q_{st}) for substrate binding, we measured isotherm data for each material at a minimum of three different temperatures. Initial attempts to fit the adsorption isotherm data to the Dual-Site Langmuir model (eq. 1) resulted in a poor fit in the low-pressure region (**Figure S11**) producing heat of adsorption values (**Figure S12**) of questionable accuracy. As a result, the adsorption isotherms at three temperatures were simultaneously fitted to a Virial-type expression (eq. 2).[2] The virial model has been extensively used to calculate heats of adsorption from isotherm data as the isotherms plot coverage as a function of pressure and provides more reasonable values of Q_{st} irrespective of the adsorption mechanism.[3] Fitting with the virial-equation provided better low pressures fits (**Figure S13**).

$$n = \frac{q_A b_A P}{1 + b_A} + \frac{q_B b_B P}{1 + b_B} \tag{1}$$

$$\ln p = \ln n + \left(\frac{1}{T}\right) \sum_{i=0}^{m} a_i n^i + \sum_{i=0}^{n} b n^i \tag{2}$$

$$Q_{st} = -R \sum_{i=0}^{m} a_i N^i \tag{3}$$

The fitting parameters for each adsorbent is given below the respective figure. The number of virial coefficients was considered satisfactory when the fit did not improve with added a or b parameters. The quality of the fit was evaluated by comparing adjusted R^2 values and the residual sum of squares, in addition, to visually inspection of the fit. It should be noted; some fits feature significant derivations between the virial model and the experimental data at higher pressures. The values of the virial coefficients a_0 through a_m were then used to calculate the isosteric heat of adsorption using equation 3.

For CO_2 adsorption of MFU-4l, the heat of adsorption at the zero-coverage limit was also calculated from the Henry's constant K_H (cm g^{-1} kPa^{-1}), which can be determined from the linear region of the isotherm at very low pressures. In the linear region the amount adsorbed follows Henry's Law (eq. 4). The heat of adsorption is calculated using the Clausius-Clapeyron equation.

$$n = K_H P \tag{4}$$
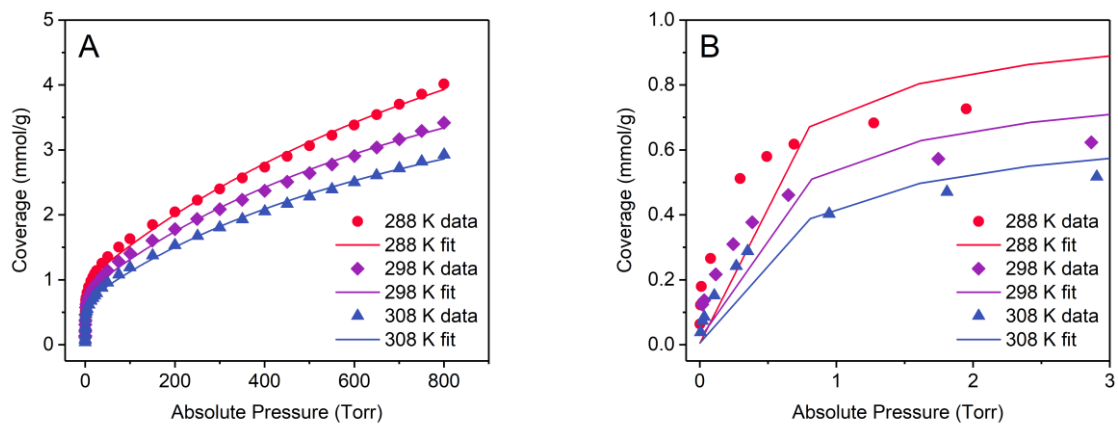
CO₂ adsorption for MFU-4l-(OH)

Figure S11. CO$_2$ adsorption isotherms of **2** measured at 288 K (red circles), 298 K (purple diamonds), and 308 K (blue triangles). (A) shows the full pressure range and (B) shows the low-pressure region. The symbols represent data and the lines represent the DSL model fit. Given the poor fits at low pressure, the DSL model provided an unreasonable Q_{st} (**Figure S12**). As a result, we did not use the DSL model to determine the Q_{st}.
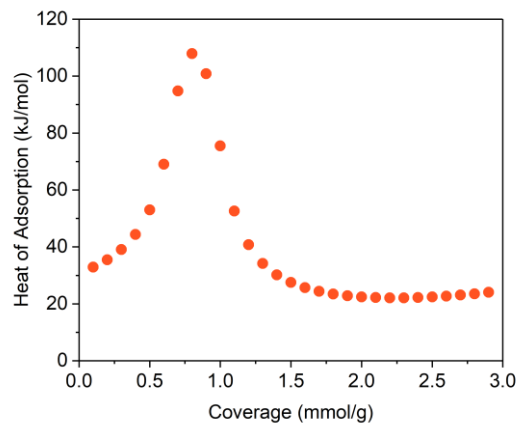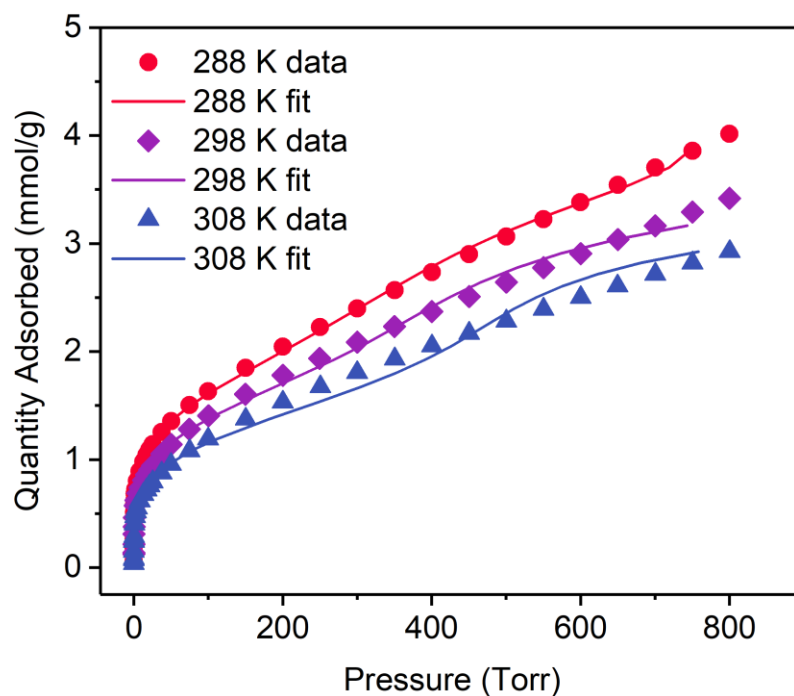
Figure S12. Coverage-dependent CO_2 adsorption enthalpy for **2** as obtained from Dual-Site Langmuir model of the CO_2 sorption isotherms. The poor fit in the low-pressure region indicates the heat of adsorption between 0 and 1 mmol/g coverage is of questionable accuracy.

Figure S13. CO_2 adsorption isotherms of **2** measured at 288 K (red circles), 298 K (purple diamonds), and 308 K (blue triangles). The lines represent the Virial fitting of the adsorption isotherms.

Table S3. Virial fitting parameters for the adsorption of carbon dioxide by MFU-4*l*-(OH).

index	ai	bi	Standard Error ai	Standard Error bi
0	-9730.85061	29.74961	726.0938	2.42089
1	541.98762	7.09937	1978.2961	6.57413
2	3045.31104	-12.86594	1459.1224	4.78533
3	-973.31472	2.91462	339.78303	0.98805
4	83.64366		49.61208	
5	-9.7301		5.08917	
R^2	0.9971			
chi squared	0.0377			
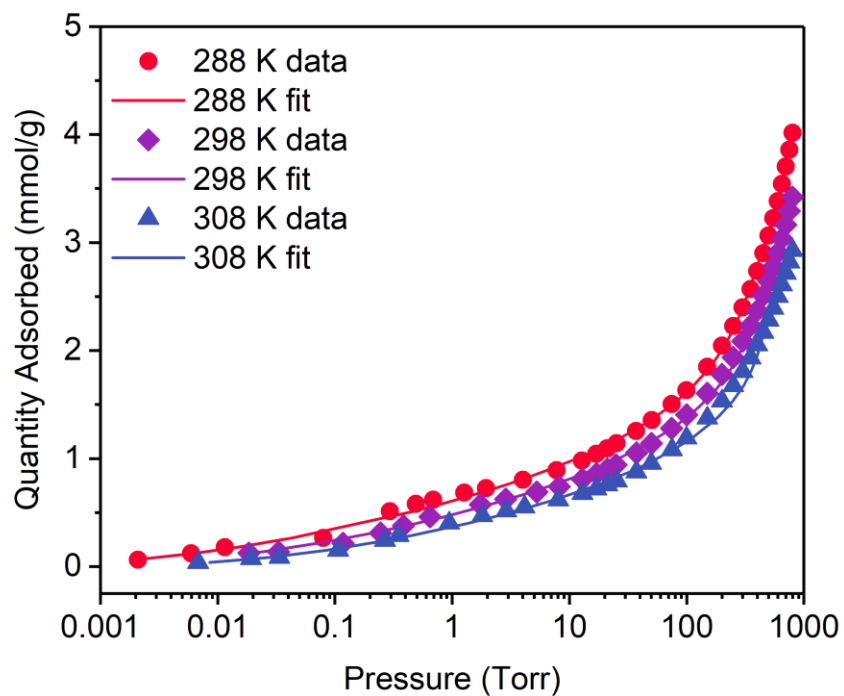
Figure S14. CO_2 adsorption isotherms of **2** measured at 288 K (red circles), 298 K (purple diamonds), and 308 K (blue triangles). The logarithmic scale is shown to display the good fit at low pressures. The lines represent the Virial fitting of the adsorption isotherms.
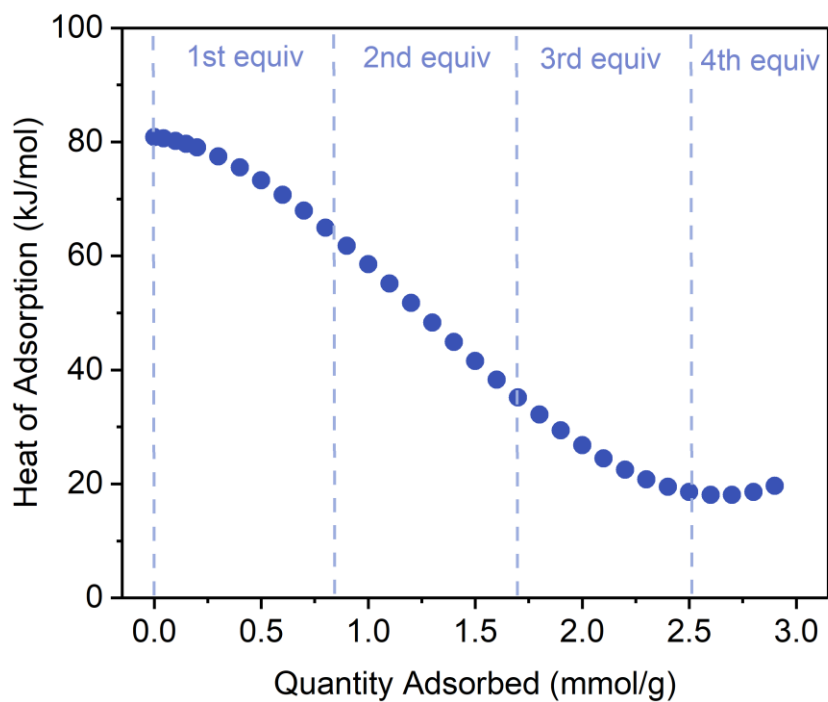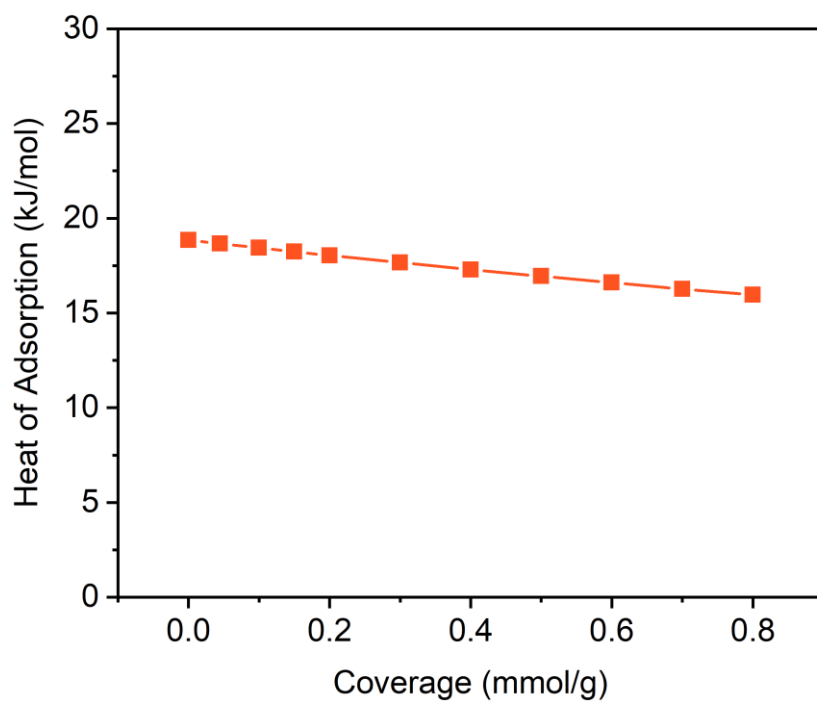
Figure S15. Coverage-dependent CO_2 adsorption enthalpy for **2** as obtained from fitting the Virial equation to three different temperature CO_2 isotherms. The lines indicate the number of equivalents of CO_2 per metal node (1st equiv., 0.85 mmol/g; 2nd equiv., 1.70 mmol/g; 3rd equiv., 2.55 mmol/g). The total number of Zn—OH sites is 3.41 mmol/g.

CO₂ adsorption MFU-4*l*
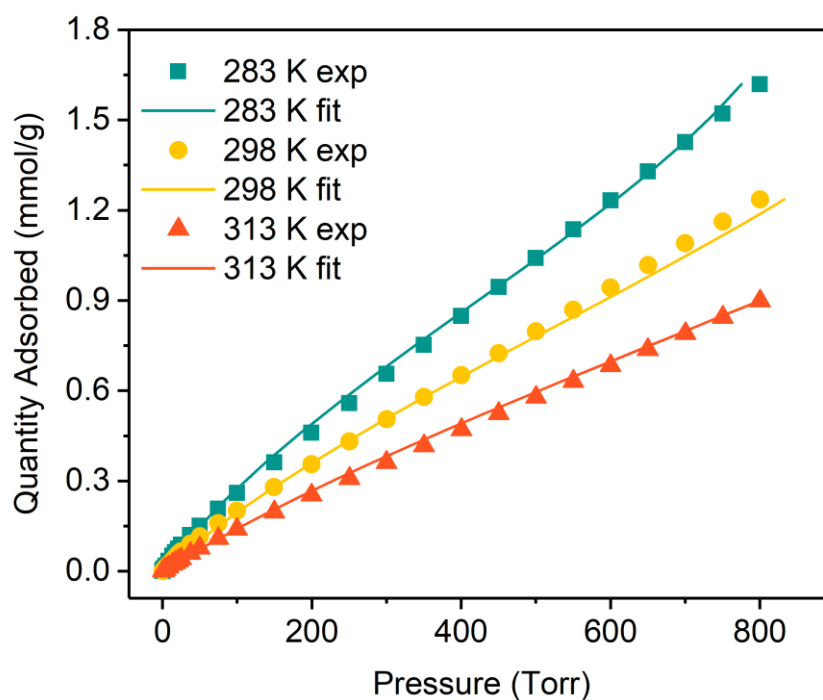
Figure S16. CO₂ adsorption isotherms of **1** measured at 283 K (turquoise squares), 298 K (yellow circles), and 313 K (orange triangles). The lines represent the Virial fitting of the adsorption isotherms.

Table S4. Virial fitting parameters for the adsorption of carbon dioxide by **1**.

index	ai	bi	Standard Error ai	Standard Error bi
0	-2266.96577	13.72805	298.39770	1.00388
1	497.43778	-1.02126	677.18815	2.18717
2	-79.71544		57.70613	
R^2	0.9879			
chi squared	0.0758			

Figure S17. Coverage-dependent CO_2 heat of adsorption for **1** as obtained from fitting the Virial equation to three different temperature CO_2 isotherms. The Q_{st} at zero coverage is 18.8 kJ/mol.
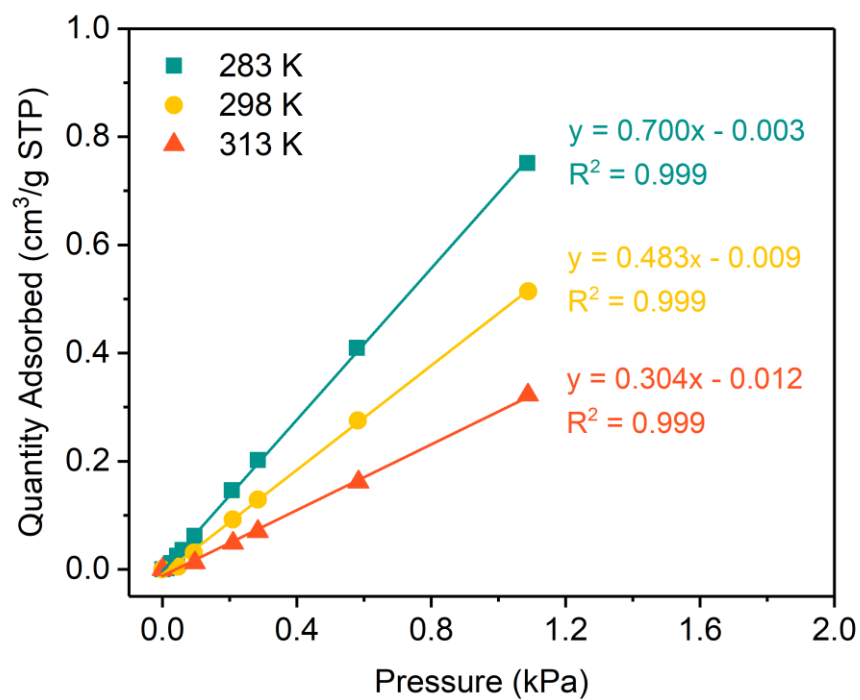
Figure S18. Determination of the Henry's constant for CO_2 adsorption in MFU-4*l* (**1**).
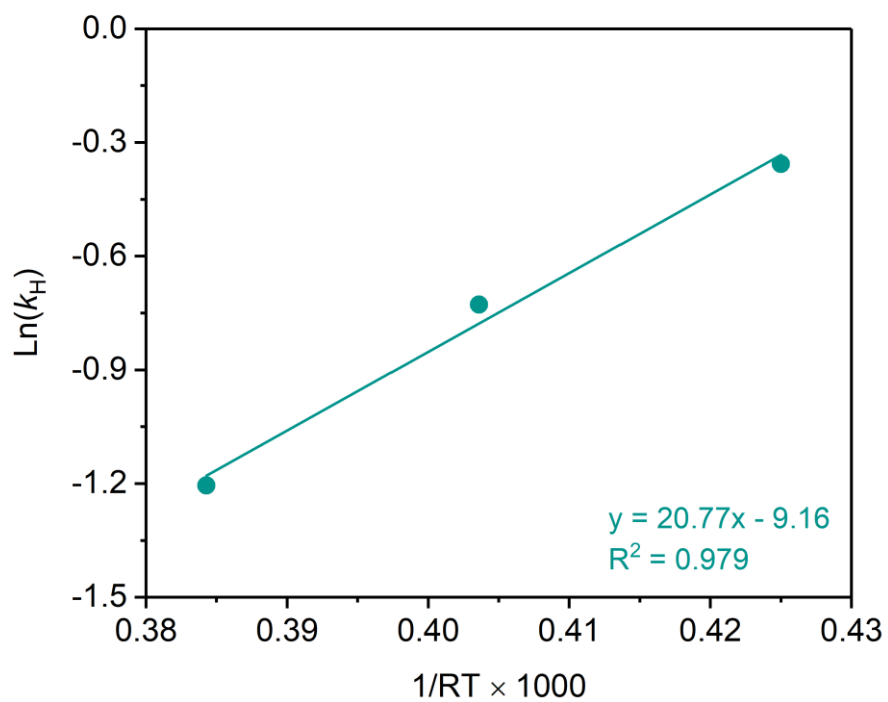
Figure S19. $\ln K_H$ versus $1/RT$ plots for CO_2 adsorption in MFU-4l. Using Henry's constant method, the heat of adsorption at zero coverage is 20.8 ± 2 kJ/mol.

Diffuse Reflectance IR Spectroscopy
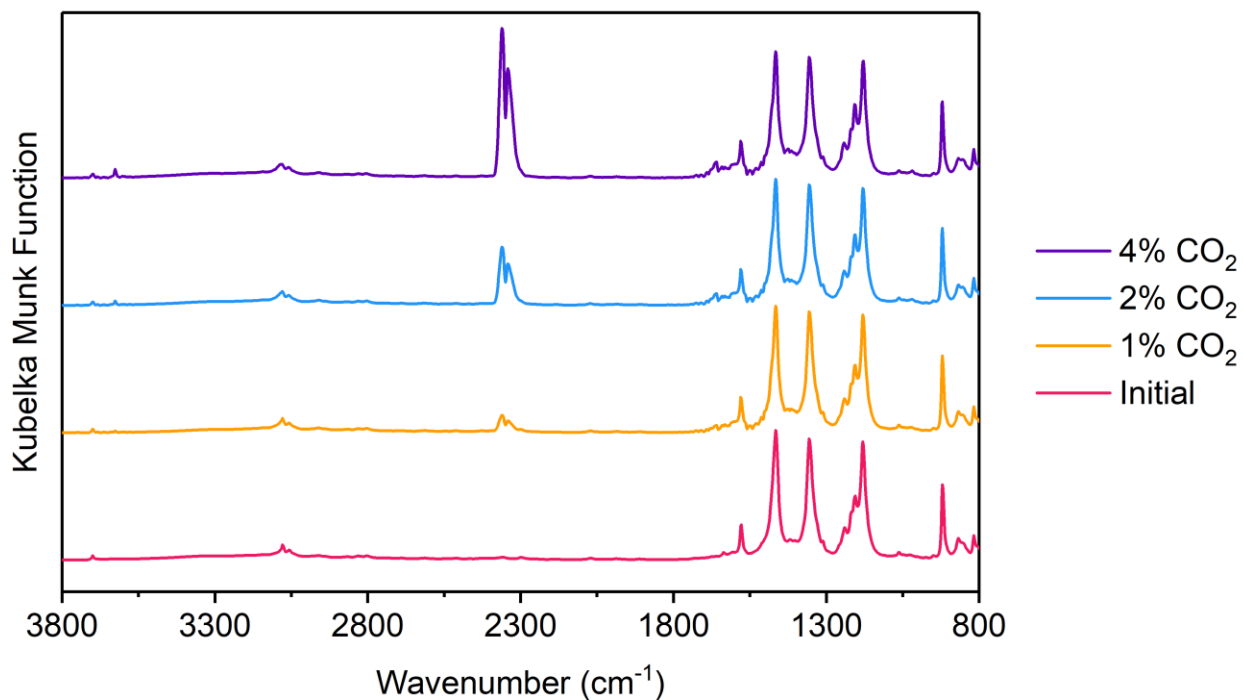
Figure S20. DRIFT spectra for CO_2 adsorption by MFU-4*l*-(OH) (**2**) at different concentrations of CO_2. The concentration was increased from 1 to 2 to 4%. The difference spectrum in Figure S21 reveals the formation of bicarbonate ligand.
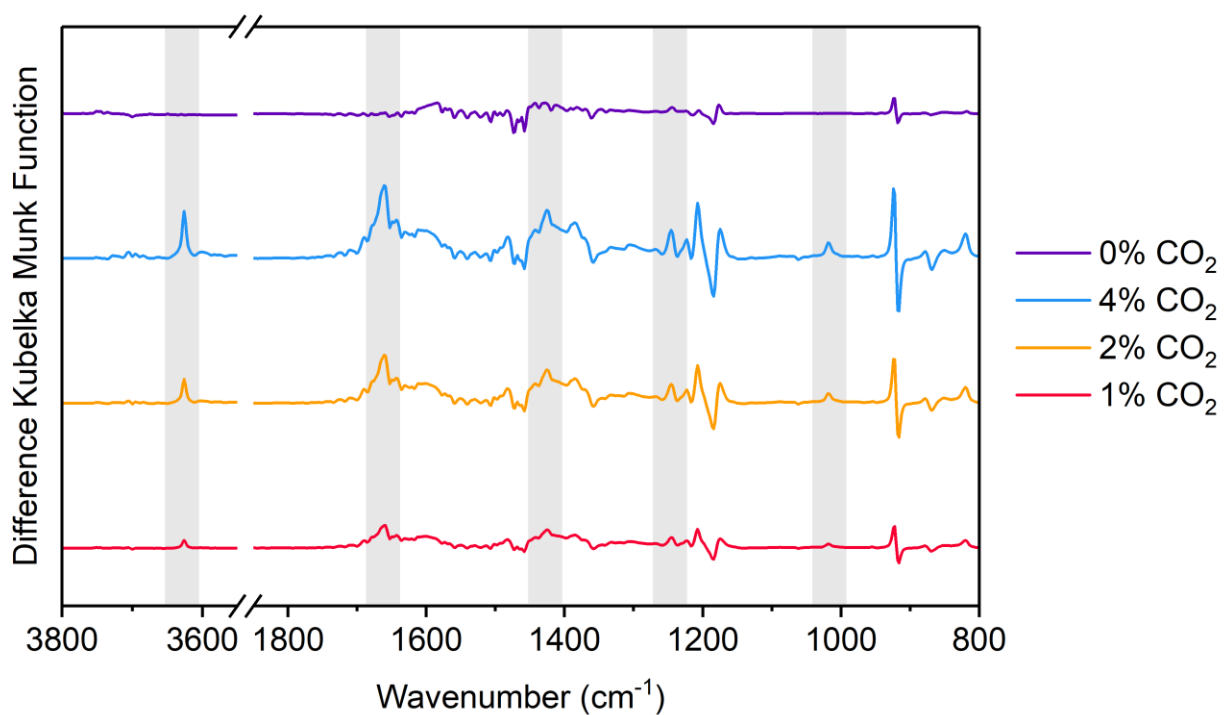
Figure S21. Difference DRIFT spectra for CO_2 adsorption by MFU-4*l*-(OH) (**2**) at different concentrations of CO_2 in argon. The concentration was increased from 1 to 2 to 4% and then decreased to 0% CO_2. The shaded areas represent new bands that grow in with increasing CO_2 concentration that are associated with a Zn—CO_3H group, notably, these disappear when exposed to 100% argon flow.
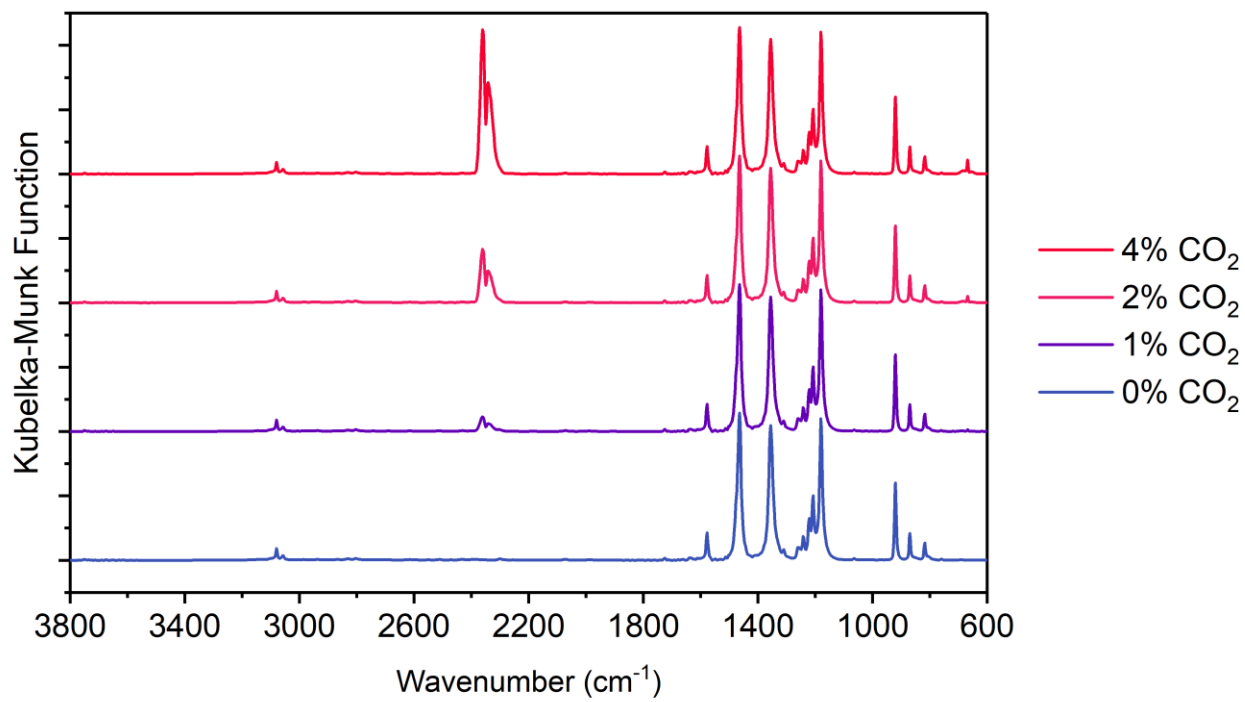
Figure S22. DRIFT spectra of MFU-4l (**1**) with increasing concentrations of CO_2. The peak at 2362 cm^{-1} is the asymmetric stretch of gaseous CO_2 and indicates no reaction with the MFU-4l framework. The difference spectrum is given below in Figure S23.
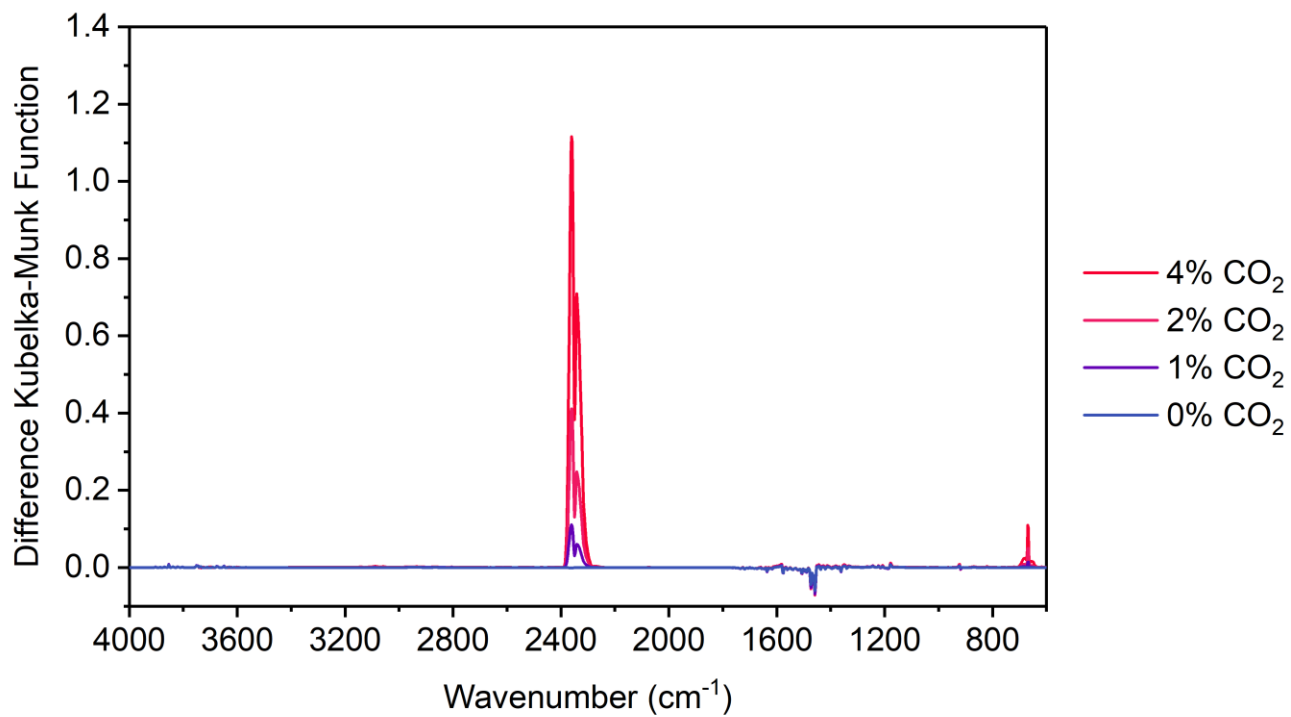
Figure S23. Difference DRIFT spectra of MFU-4*l* (**1**) under increasing concentrations of CO_2. The peak at 2362 cm^{-1} is the asymmetric stretch of gaseous CO_2. No other peaks are observed indicating no reaction between CO_2 and MFU-4*l*.

Water Stability of MFU-4*l*-(OH)

MFU-4*l*-(OH) was submerged in water for a set period (6 & 24 hours) and then analyzed by powder X-ray diffraction. Prior to recording the PXRD pattern, the material was washed with methanol (3 × 2 mL) to allow for better drop casting on to the ZBH plate.
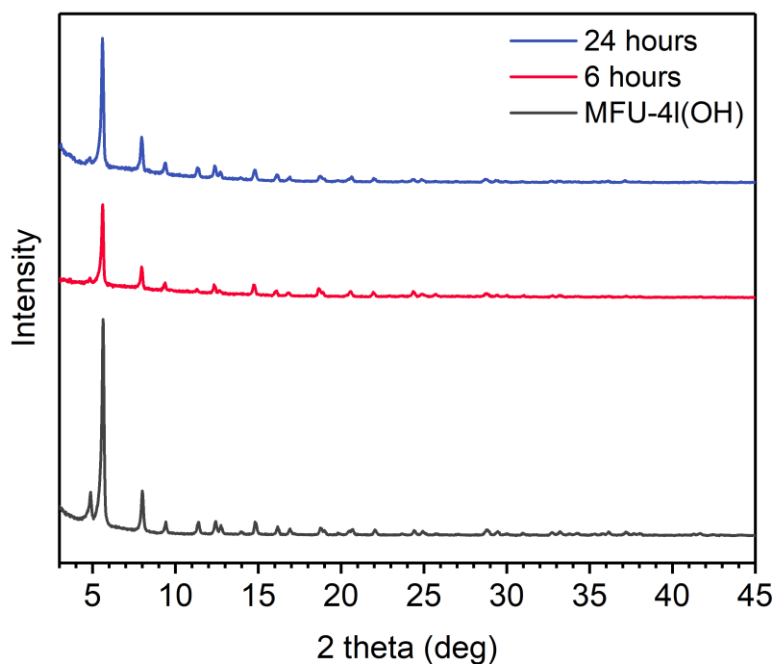

Figure S24. Powder X-ray diffraction patterns for MFU-4*l*-(OH) (grey trace), after submersion in water for 6 hours (red trace), and after submersion in water for 24 hours (blue trace). The materials remained crystalline after submersion in water.

Buffer Stability Studies

The stability of MFU-4*l*-(OH) in a variety of different buffer systems was examined. Buffer systems with pH of 8.0–9.0 were tested. A sample of MFU-4*l*-(OH) (~15 mg) was submerged in a buffer solution (3 mL) for 3 hours. The solution was decanted, and the MOF was washed with MeOH (3 × 10 mL). A material was analyzed by PXRD.

Table S5. Buffer systems tested for water stability of MFU-4*l*-(OH).

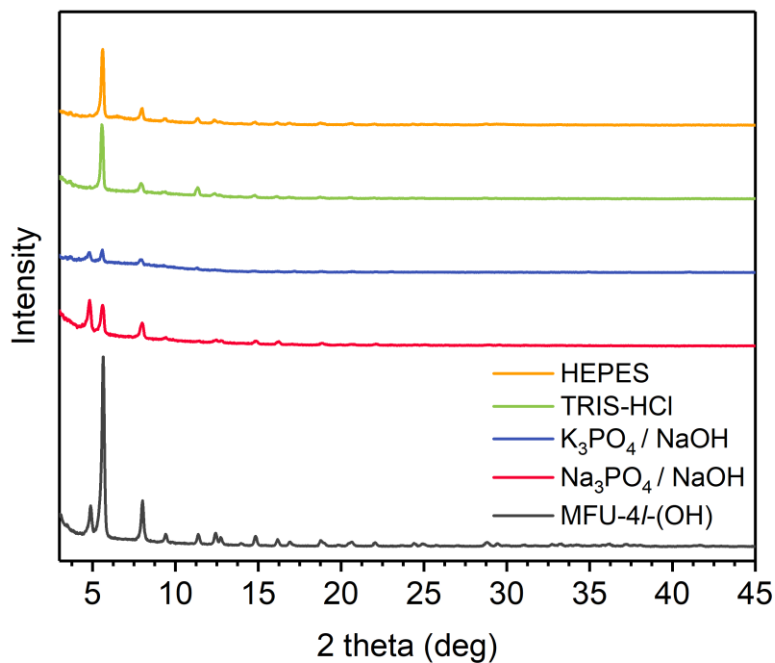| Entry	Buffer System	Buffer Concentration	pH
1	K_3PO_4 / NaOH	1.0 M	8.0
2	TRIS-HCl	1.0 M	8.0
3	$NaHCO_3$ / Na_2CO_3	0.2 M	9.0
4	HEPES	50 mM	8.0
5	Pure water	n/a	7.0

Figure S25. Powder X-ray diffraction of MFU-4*l*-(OH) (**2**) after submersion in buffer solution. After submersion in HEPES and TRIS-HCl the crystallinity is retained as indicated by the PXRD pattern. The phosphate buffers lead to a significant increase in the feature at ~4.8°, which is ascribed to the exchange of the hydroxide ligand for phosphate of the buffer. These materials exhibit IR stretches consistent with phosphate post-exposure.
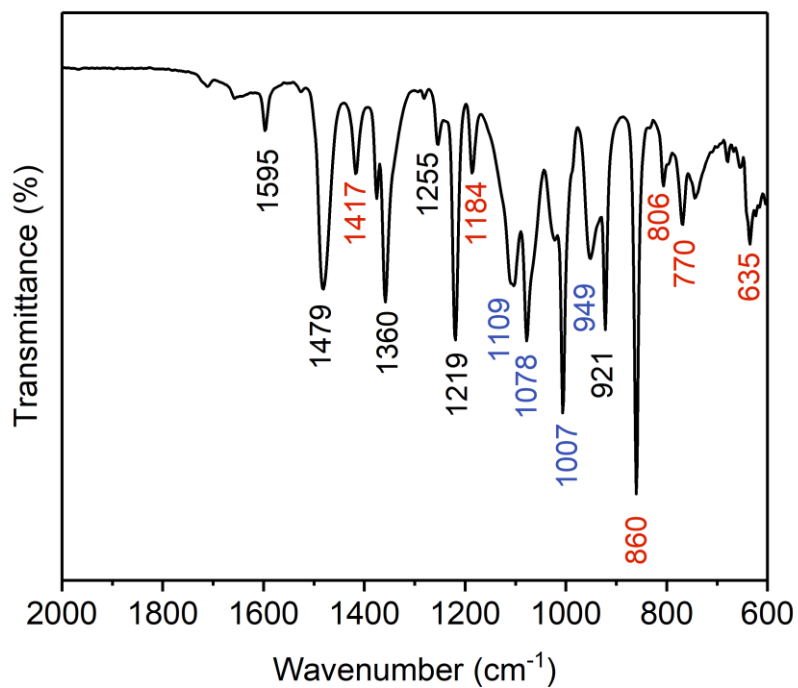
Figure S26. IR spectra of MFU-4*l*-(OH) after submersion in sodium phosphate / sodium hydroxide buffer solution. The wavenumbers marked in black are associated with the MOF framework and those marked in blue are assignable to phosphate stretches. Bands denoted by red are unknown new features.

^{18}O exchange between H_2O and CO_2 catalyzed by MFU-4*l*-(OH)

A custom-made batch reactor (**Figure S27**) was charged with MOF (~10 mg), MeCN (0.5 mL), and $H_2^{18}O$ (0.1 mL). The solution was degassed by three nitrogen / vacuum cycles, and then backfilled with CO_2 (15 psig). The distribution of carbon dioxide isotopologues was monitored periodically using gas chromatography-mass spectrometry (GC/MS). The ratio of its isotopologues, $C^{16}O2$, $C^{16,18}O_2$, and $C^{18}O_2$, was determined from the relative abundances of *m/z* 44, 46, and 48 in the mass spectrum.
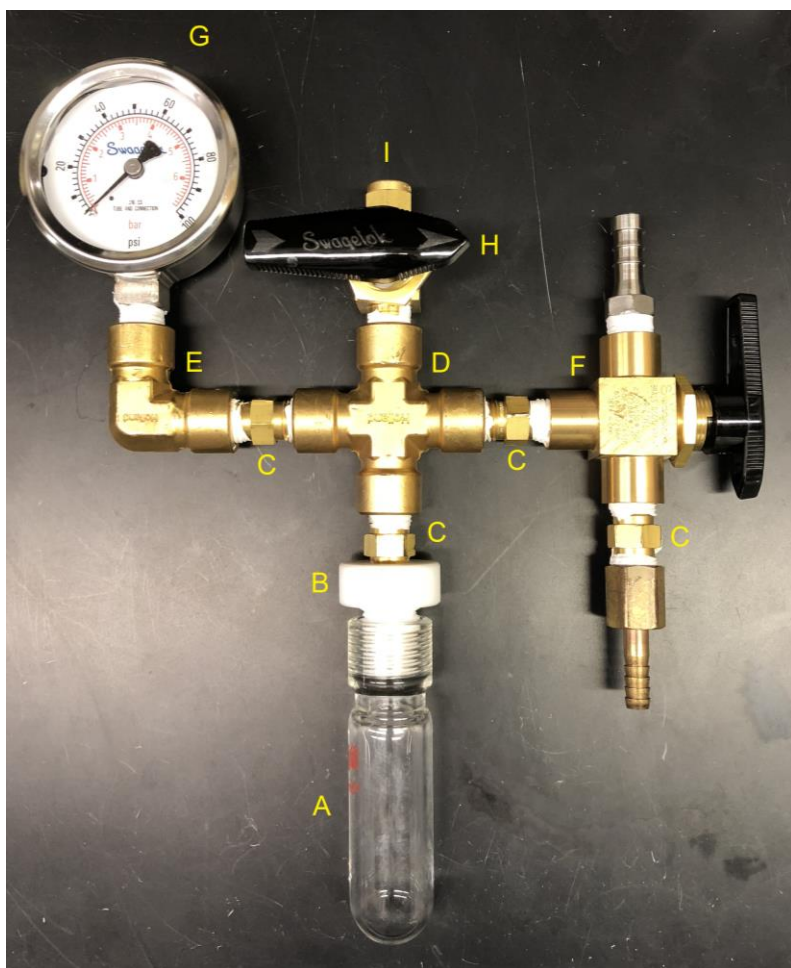
Figure S27. Picture of the custom-made reactor setup. (A) 15 mL Pressure Tube (Ace Glass, 8648 product family); (B) Adapter NPT tubing to Ace-Thred (Ace Glass, 5844-74); (C) ¼" Brass Male Hex Nipple NPT (Swagelok, B-4-HN); (D) Brass Pipe Fitting, Cross ¼", Female NPT (Swagelok, B-4-CS); (E) Brass Pipe Elbow ¼", Female NPT (Swagelok, B-4-E); (F) Brass 1-Piece 40 Series 3-way Ball Valve (Swagelok, B-43XF4); (G) 100 psig SS Gauge (Swagelok, PGI-63C-PG100-LAOX); (H) Brass 1-Piece 40 Series Ball Valve (Swagelok, B-43M4-S4); (I) Septum 9.5 mm.
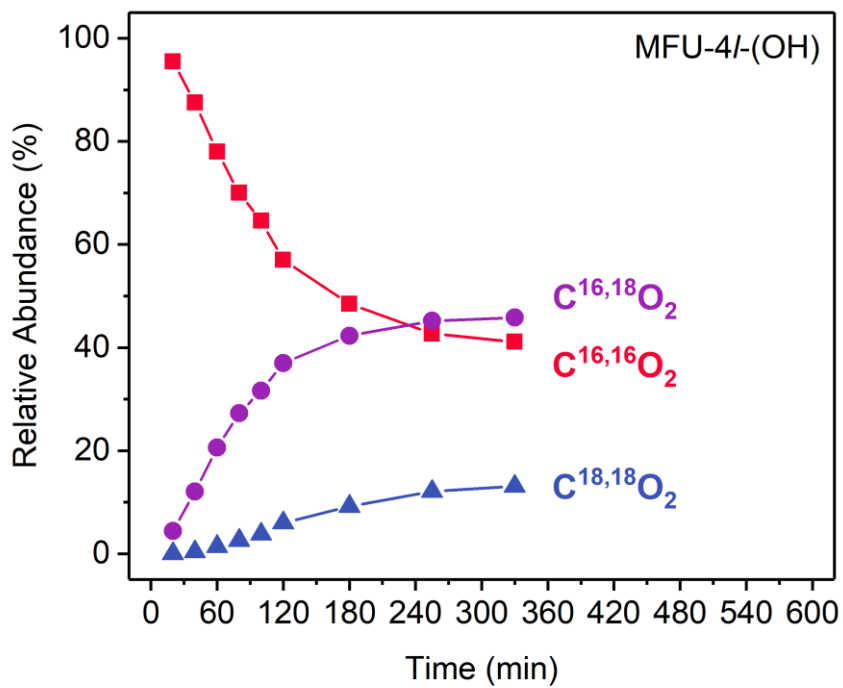
Figure S28. Normalized relative abundance of the carbon dioxide isotopologues upon exposure of carbon dioxide to $H_2{}^{18}O$ and MFU-4*l*-(OH) (**2**) in MeCN. Time taken to reach an equilibrium mixture of CO_2 isotopologues was 5.5 hours.
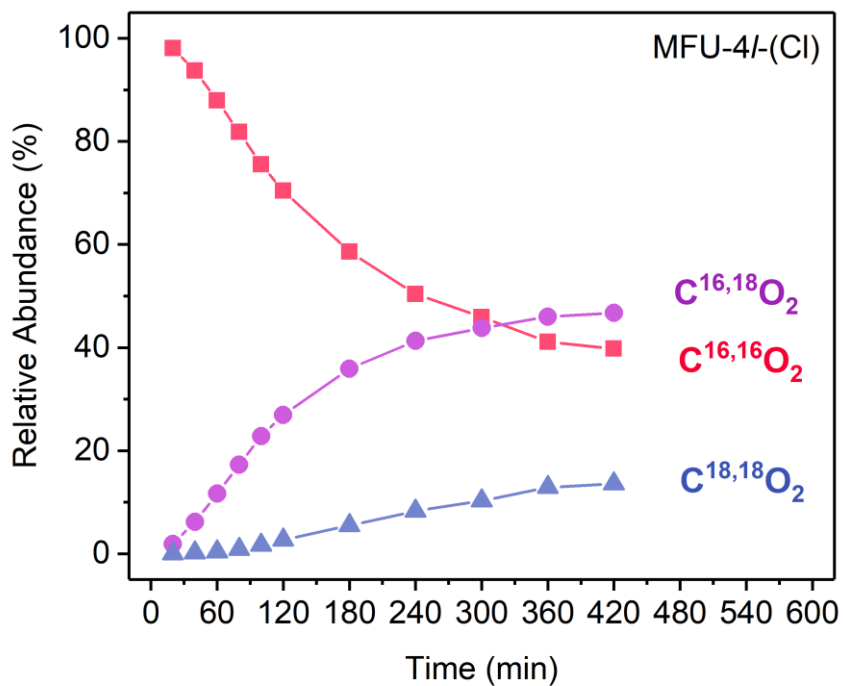
Figure S29. Normalized relative abundance of the carbon dioxide isotopologues upon exposure of carbon dioxide to $H_2{}^{18}O$ and MFU-4*l*-(Cl) (**1**) in MeCN. Time taken to reach an equilibrium mixture of CO_2 isotopologues was ~7 hours.
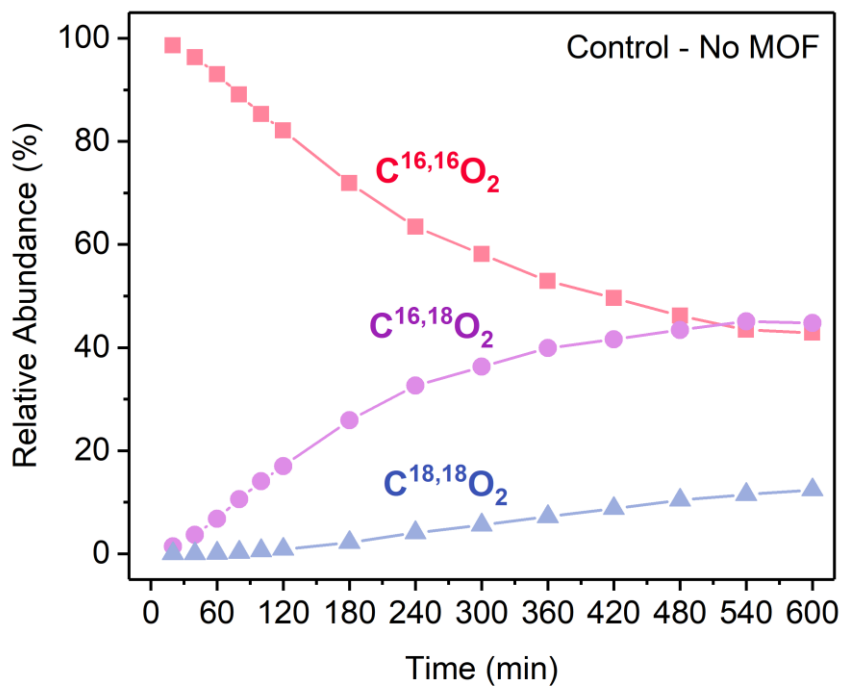
Figure S30. Relative abundance of the carbon dioxide isotopologues versus time for the control reaction between $H_2^{18}O$ and CO_2 in MeCN.
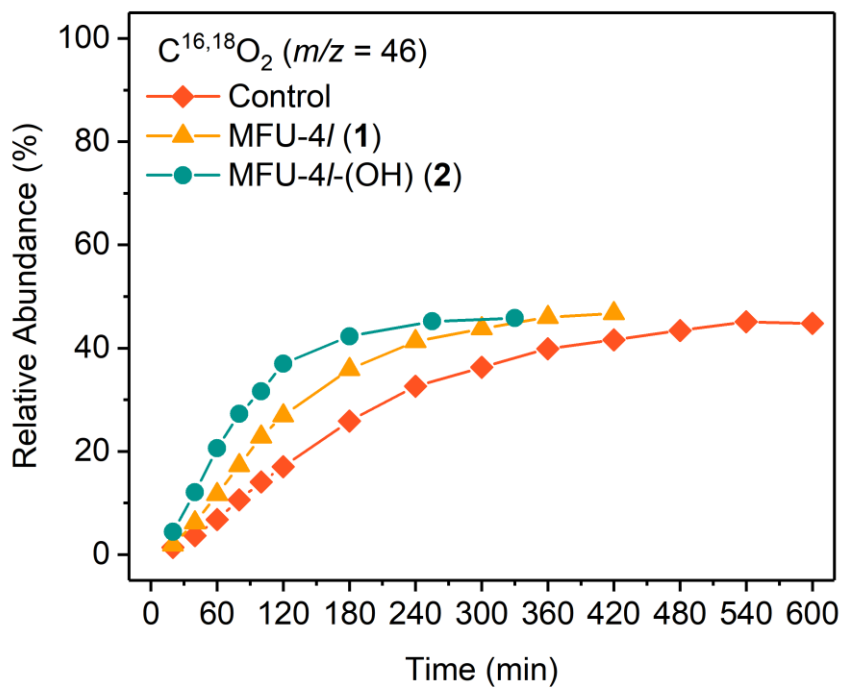
Figure S31. Comparison of the increase in relative abundance of $C^{16,18}O_2$ for reactions with **1**, **2**, and the control.

Catalytic hydrolysis of 4-nitrophenyl acetate

    The hydrolysis reactions were performed in 50 mL centrifuge tubes with added 4-NPA in acetonitrile and 50 mM HEPES buffer solution. The concentration of 4-nitrophenol was monitored by time-dependent UV-vis spectroscopy by measuring its absorption band at 405 nm. A calibration curve was first prepared using known quantities of 4-nitrophenol in 50 mM HEPES solution.
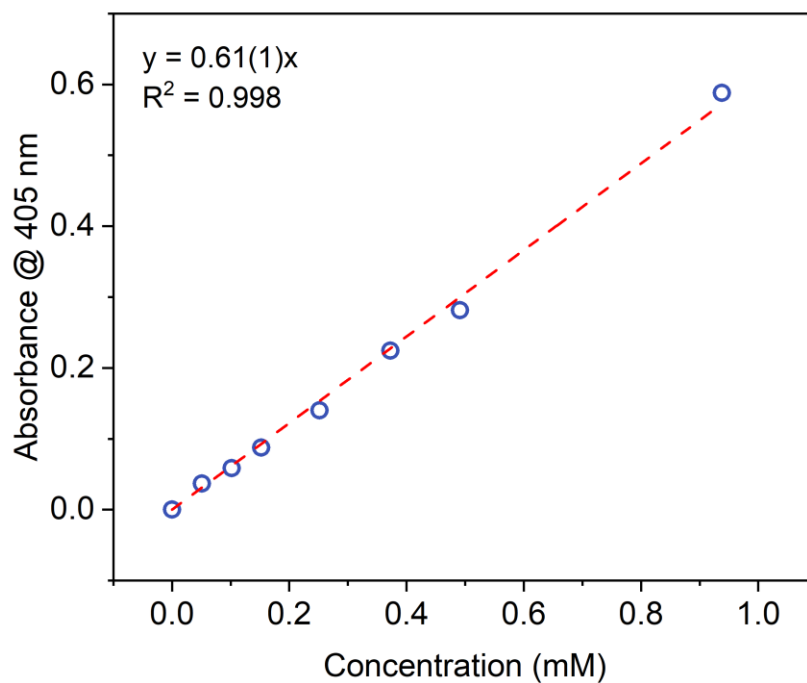

Figure S32. Calibration curve for 4-nitrophenol in 50 mM HEPES buffer solution. The calculated extinction coefficient is 627 M^{-1} cm^{-1}.
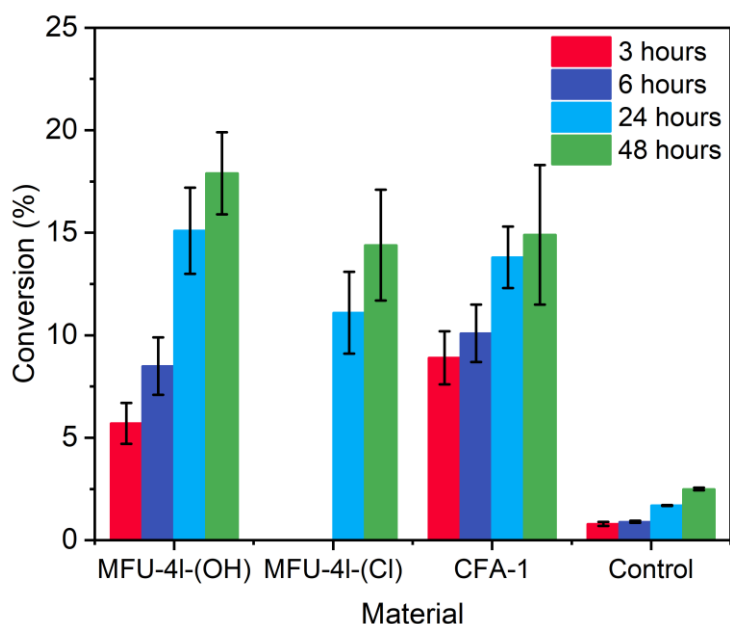
Figure S33. The percent conversion of 4-nitrophenyl acetate to 4-nitrophenol under four different conditions (catalysts: MFU-4*l*-(OH) (**2**), MFU-4*l* (**1**), CFA-1, and control) at four different time points (3, 6, 24, and 48 hours). Conditions: catalyst loading, 8-10 mol% (MFU-4*l*-(OH) (**2**) and MFU-4*l* (**1**)) or 12-14 mol% (**CFA-1**), 50 mM HEPES buffer, 1 mM 4-NPA. The mol% catalyst is calculated from the number of peripheral Zn–X sites (four per molecular formula). Each experiment run was repeated a minimum of three times and the error bars represent one standard deviation. Small particles of MFU-4*l* interfered with UV-vis measurements at 3 and 6-hour time points in all three measurements. Notably, the control reaction indicates the hydrolysis of 4-nitrophenyl acetate occurs with very low conversion without a MOF.
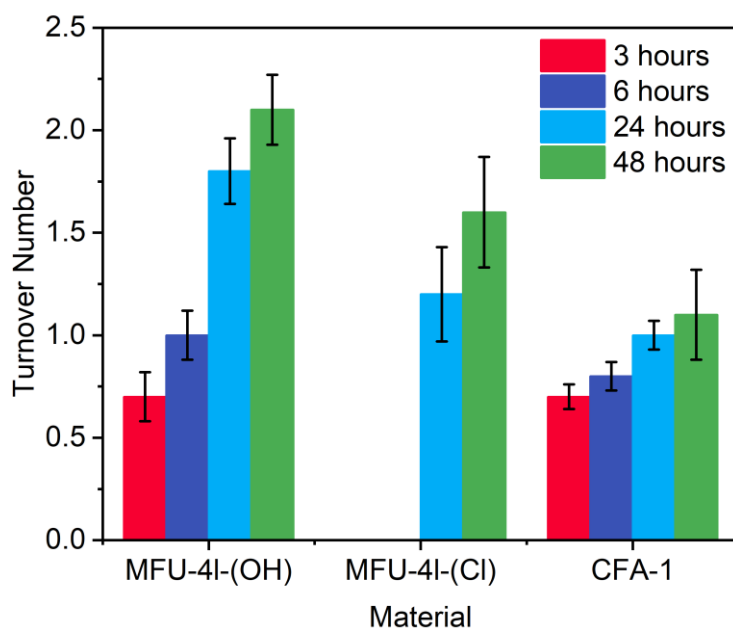
Figure S34. Turnover number of 4-nitrophenyl acetate to 4-nitrophenol under four different conditions (catalysts: MFU-4*l*-(OH), MFU-4*l*-(Cl), CFA-1, and control) at four different time points (3, 6, 24, and 48 hours). Conditions: catalyst loading, 8-10 mol% (MFU-4*l*-(OH) (**2**) and MFU-4*l* (**1**)) or 12-14 mol% (**CFA-1**), 50 mM HEPES buffer, 1 mM 4-NPA. The mol% catalyst is calculated from the number of peripheral Zn—X sites (four per molecular formula). Each experiment run was repeated a minimum of three times and the error bars represent one standard deviation.

Table S6. Data for the hydrolysis of 4-nitrophenyl acetate using different MOF catalysts.

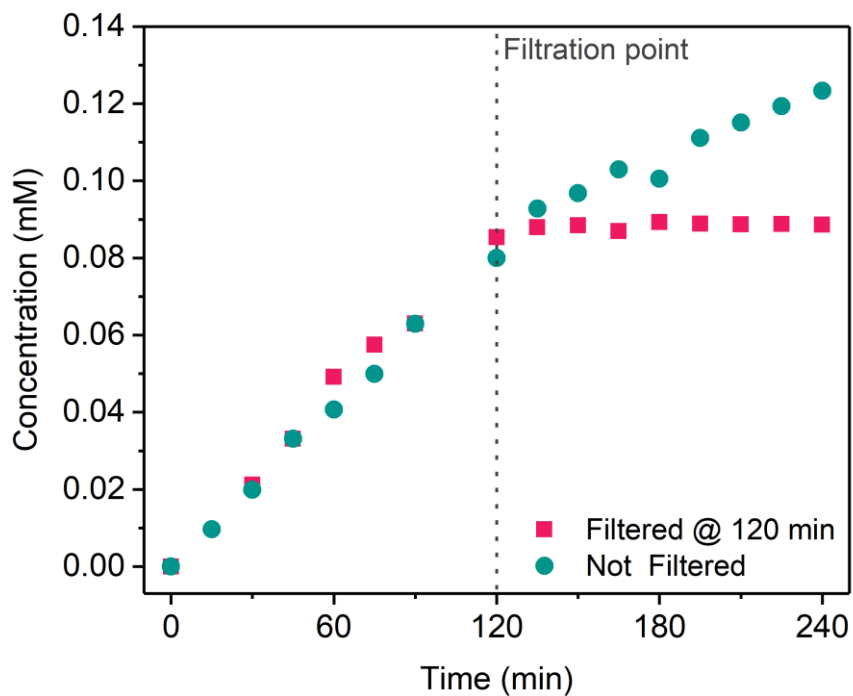| Material	Conversion (mmol/mmol) 3 hours	Conversion (mmol/mmol) 6 hours	Conversion (mmol/mmol) 24 hours	Conversion (mmol/mmol) 48 hours
Control	0.8 ± 0.1 % (n/a)	0.9 ± 0.1 % (n/a)	1.7 ± 0.2 % (n/a)	2.5 ± 0.1 % (n/a)
MFU-4*l*-(OH)	5.7 ± 1.0 % (0.7 ± 0.1)	8.5 ± 1.4 % (1.0 ± 0.1)	15.1 ± 2.1 % (1.8 ± 0.2)	17.9 % ± 2.1 (2.1 ± 0.2)
MFU-4*l*-(Cl)	n/a	n/a	11.1 ± 2.2 % (1.2 ± 0.2)	14.4 ± 2.7 % (1.6 ± 0.3)
CFA-1	8.9 ± 1.4 % (0.7 ± 0.1)	10.1 ± 1.4 % (0.8 ± 0.1)	13.8 ± 1.5 % (1.0 ± 0.1)	14.4 ± 2.7 % (1.6 ± 0.3)

Figure S35. Change in absorbance over time for the hydrolysis of 4-nitrophenyl acetate in the presence of MFU-4*l*-(OH) (**2**). Two reaction vessels were charged with 45 mL of 50 mM HEPES buffer and 5 mL of 4-nitrophenyl acetate in acetonitrile ([4-NPA] = 1 mM, 0.05 mmol) and **2** (3 mg, 0.003 mmol, 24 mol% per Zn-OH site). One reaction flask was filtered after 120 minutes and the other was left as is. The reaction was monitored by tracking the 405 nm signal of 4-nitrophenol by UV-vis spectroscopy. The observed initial reaction rate is 0.7 µM/min.

Computational Details

General Comments. Computations were performed using the VASP[4] (extended solids) or Gaussian 09 (molecular) software.[5] The PBE functional was used for both molecular and solid-state calculations.[6] A 500 eV planewave cutoff and Gamma-only k-grid was used for the solid-state calculations. The Pople basis set 6-311G** was used for molecular calculations.[7] MFU-4l-(OH) (**2-DFT**) and $Zn_5(OH)_4(BTA)_3$ (BTA = benztotriazole) were geometrically optimized starting from the crystallographically determined MFU-4l and $Zn_5Cl_4(BTA)_3$ xyz coordinates but with the Cl replaced by OH groups. Simulated IR spectra were recovered from the $Zn_5(OH)_4(BTA)_3$ cluster optimizations (**Figure S36**). The XYZ coordinates for all computed structures are provided in an Excel document (**Table S8**).

CO_2 insertion. Binding energies were calculated from the difference in energy between the MOF or cluster after bicarbonate formation and the sum of the MOF or cluster with one less bicarbonate and free CO_2. Due to computational expense, we were not able perform full optimizations on the bulk solid-state material after CO_2 additions, and instead only allowing the local node-bicarbonate structure to relax. There was reasonably good agreement between the molecular and solid-state bicarbonate formation enthalpies of the first addition of CO_2 (–50.4 and –60.7 kcal/mol, respectively). The disparity is due to our constrained relaxation parameters. Binding enthalpies of subsequent CO_2 additions to the $Zn_5(OH)_4(BTA)_3$ cluster were performed with full optimization and were found to be less favored than the first addition, ranging from –42.0 to –37.8 kcal/mol (**Table S7**), which qualitatively agrees with the decreasing heat of adsorption determined experimentally.

Table S7. Binding enthalpies for sequential addition of CO_2 to $Zn_5(OH)_4(bibta)_3$ cluster.

Addition of CO_2	Binding Energy (kJ/mol) using PBE/6-31G**	Binding Energy (kJ/mol) using PBE/6-311G**
First	–56.7	–50.4
Second	–48.2	–42.0
Third	–48.6	–42.0
Fourth	–46.1	–37.8
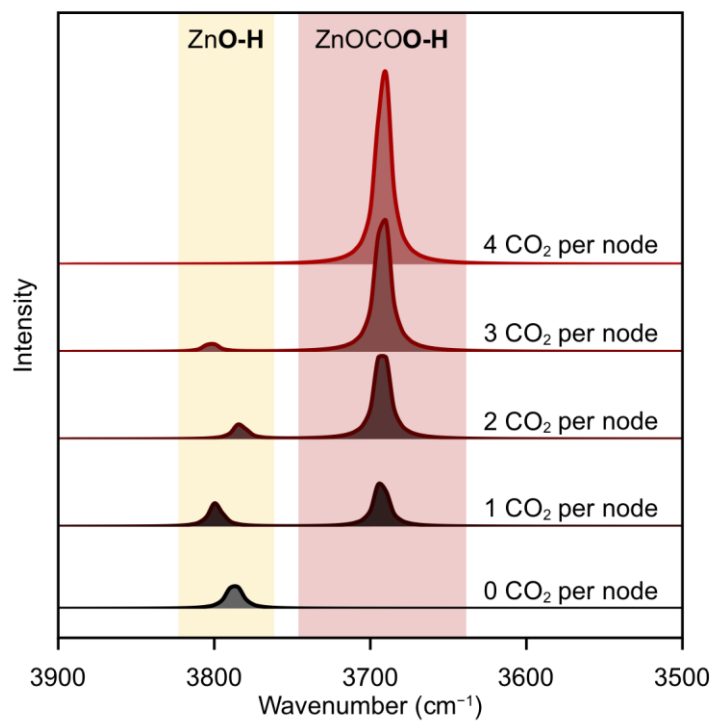
Figure S36. Simulated IR spectra for $Zn_5(OH)_{4-n}(CO_3H)_n(BTA)_3$ (n = 0–4). The unscaled vibrational frequencies are shown for the Zn**O–H** and ZnOCO**O–H**. The variation of the Zn-OH is due to variation in the symmetry of the cluster.

References

[1] Denysenko, D., Grzywa, M., Tonigold, M., Streppel, B., Krkljus, I., Hirscher, M., Mugnaioli, E., Kolb, U., Hanss, J., and Volkmer, D. Elucidating gating effects for hydrogen sorption in MFU-4-type triazolate-based metal-organic frameworks featuring different pore sizes. *Chem. Eur. J.* **2011**, *17*, 1837–1848.

[2] Czepirski, L., and Jagiello, J. Virial-type thermal equation of gas-solid adsorption. *Chem. Eng. Sci.* **1989**, *44*, 797–801.

[3] Dinc. , M., Dailly, A., Liu, Y., Brown, C.M., Neumann, D.A., and Long, J.R. (2006). Hydrogen Storage in a Microporous Metal−Organic Framework with Exposed Mn^{2+} Coordination Sites. *J. Am. Chem. Soc.* **2006**, *128*, 16876–16883.

[4] Kresse, G.; Furthmuller, J. Efficient Iterative Schemes for Ad Initio Total-Energy Calculations using a Plane-Wave Basis Set. *Phys. Rev. B.* **1996**, *54*, 11169–11186.

[5] Gaussian 09, Revision D.02, M. J. Frisch, G. W. Trucks, H. B. Schlegel, G. E. Scuseria, M. A. Robb, J. R. Cheeseman, G. Scalmani, V. Barone, G. A. Petersson, H. Nakatsuji, X. Li, M. Caricato, A. Marenich, J. Bloino, B. G. Janesko, R. Gomperts, B. Mennucci, H. P. Hratchian, J. V. Ortiz, A. F. Izmaylov, J. L. Sonnenberg, D. Williams-Young, F. Ding, F. Lipparini, F. Egidi, J. Goings, B. Peng, A. Petrone, T. Henderson, D. Ranasinghe, V. G. Zakrzewski, J. Gao, N. Rega, G. Zheng, W. Liang, M. Hada, M. Ehara, K. Toyota, R. Fukuda, J. Hasegawa, M. Ishida, T. Nakajima, Y. Honda, O. Kitao, H. Nakai, T. Vreven, K. Throssell, J. A. Montgomery, Jr., J. E. Peralta, F. Ogliaro, M. Bearpark, J. J. Heyd, E. Brothers, K. N. Kudin, V. N. Staroverov, T. Keith, R. Kobayashi, J. Normand, K. Raghavachari, A. Rendell, J. C. Burant, S. S. Iyengar, J. Tomasi, M. Cossi, J. M. Millam, M. Klene, C. Adamo, R. Cammi, J. W. Ochterski, R. L. Martin, K. Morokuma, O. Farkas, J. B. Foresman, and D. J. Fox, Gaussian, Inc., Wallingford CT, 2016.

[6] Perdew, J. P.; Burke, K.; Ernzerhof, M.; Generalized Gradient Approximation Made Simple *Phys. Rev. Lett.* **1996**, *77*, 3865-3868.

[7] Krishnan, R.; Binkley, J. S.; Seeger, R.; Pople, J. Self-consistent molecular orbital methods. XX. A basis set for correlated wave functions. *J. Chem. Phys.* **1980**, *72*, 650-654.